ABSTRACT

Dissertation Title: RESEARCH AND DEVELOPMENT OF THIN GARNET FILM BASED MAGNETO-OPTICAL IMAGERS.

Sergiy Tkachuk, Ph.D., 2011

Dissertation Directed by: Professor of Engineering Isaak D. Mayergoyz, Electrical and Computer Engineering Department

This dissertation deals with the use of magnetic single-crystal bismuth-substituted iron garnet thin films for magneto-optical imaging (MOI) of stray magnetic fields. The main advantages of such garnet-based imagers are their high sensitivity, high contrast and possibility to design films for imaging of magnetic fields in a wide range of magnitudes. The garnet films have been grown by the liquid phase epitaxy method from a flux melt on (210)- and (100)-oriented substrates and extensively characterized using various magnetic and optical methods.

Specific melt compositions are identified that allow the growth of high sensitivity and high contrast indicator films on (210)-oriented substrates. Very low saturation field

and high sensitivity of such garnet films are attributed to the existence of the so-called "easy plane of magnetization", a plane for which the magnetic free energy density is at a minimum for any orientation of the magnetization vector within this plane.

Etching has been extensively used to investigate the effect of intrinsic film domain structures on the quality of MO imagers. It has been determined that the size of the domains reduces as the thickness of the film gets smaller. Below 1μm film thickness, the domains start evolving towards the "single domain" state which is beneficial for imaging purposes. The comparison of the imaging capabilities of the etched films grown on (210)- and (100)-oriented substrates has been performed and the resolution of the (100)-oriented imagers has been found to be inferior to the imagers based on the (210)-oriented samples with an easy plane of magnetization.

The possibilities to enhance magneto-optic effects by strong local electric fields from optically induced plasmon resonances in gold nanoparticles embedded in garnet media are analyzed. The experimental investigation of the plasmon resonance enhancement of the Faraday effect has been performed and about 50% increase in Faraday rotation angle at a wavelength of 633 nm has been measured for the samples of interest. It is expected that under ideal conditions of the plasmon resonance excitation as well as proper garnet film parameters, an increase in Faraday rotation up to 400% could be achieved.

RESEARCH AND DEVELOPMENT OF THIN GARNET FILM BASED MAGNETO-OPTICAL IMAGERS.

By

Sergiy Tkachuk.

Dissertation submitted to the Faculty of the Graduate School of the
University of Maryland, College Park, in partial fulfillment
of the requirements for the degree of
Doctor of Philosophy
2011

Advisory Committee:
Professor Isaak D. Mayergoyz, Chair
Professor Romel Gomez
Professor Thomas Murphy
Professor Lourdes Salamanca-Riba
Professor Julius Goldhar
Professor Martin Peckerar

Dedication

I dedicate this dissertation to the following people:

- *The memory of my mother, who emphasized the importance of education and loved me unconditionally throughout her life.*
- *My father, for his support and prayers.*
- *My loving and patient wife, who has put up with these many years of my study.*

Acknowledgements

I would like to express my gratitude to all those who gave me the possibility to work on this dissertation. I am deeply grateful to my academic advisor, Professor of Engineering Isaak D. Mayergoyz for his continuous guidance and encouragement during the years of my research work. I have been amazingly fortunate to have an adviser who taught me how to explore new ideas on my own, while his patience and support helped me to overcome difficult situations.

Dr. Charles Krafft, has been always there to listen and give advice. I am thankful to him for the detailed discussions that helped me to sort out the technical details of my work.

I would also like to thank Dr. Iulian Nistor, who spent a lot of his time and expertise on educating me in the beginning of my involvement in this research project at the Laboratory for Physical Sciences.

I am also indebted to Dr. Edward Giess (formerly with IBM Research) and Dr. Vincent Fratello (Integrated Photonics, Inc) for their assistance. Their expertise in the growth process of garnets and melt chemistry was of great help in the advance of this project.

I am grateful to Professor Oded Rabin for his help with the project on plasmon resonance enhancement of Faraday effect.

Also, I would like to express my heart-felt gratitude to my family, my parents and my wife Yuliya, whose support and patient love always keep my spirit up.

Table of Contents

List of Tables

List of Figures

List of Publications

1) C. Krafft, **S. Tkachuk**, G. Lang, D. Bowen, I.D. Mayergoyz, "Magneto-Optic Indicator Films for Forensics (invited)", accepted for on-line publication in *MRS Online Proceedings (part of Cambridge Journals Online),* January 2011.

2) **S. Tkachuk**, G. Lang, C. Krafft, O. Rabin, I.D. Mayergoyz, "Plasmon Resonance Enhancement of Faraday Rotation in Thin Garnet Films", accepted for publication in *J. Appl. Phys.,* vol. 109, 2011.

3) I.D. Mayergoyz, G. Lang, L. Hung, **S. Tkachuk**, C. Krafft, O. Rabin, "Plasmon resonance enhancement of magneto-optic effects in garnets", *J. Appl. Phys.,* vol. 107, 09A925, 2010.

4) **S. Tkachuk**, V.J. Fratello, C. Krafft, G. Lang, I.D. Mayergoyz, "Imaging Capabilities of Bismuth Iron Garnet Films with Low Growth-Induced Uniaxial Anisotropy", *IEEE Trans. Mag.*, vol. 45 (10), 4238, 2009.

5) **S. Tkachuk**, D. Bowen, C. Krafft, I.D. Mayergoyz, "Imaging capabilities of etched (100) and (210) garnet films", *J. Appl. Phys.,* vol. 105, 07A524, 2009.

6) **S. Tkachuk**, D. Bowen, C. Krafft, I.D. Mayergoyz, "Controllability of Anisotropy of Bi and Pr Containing Garnet Films Grown on (210)-oriented Substrates", *IEEE Trans. Mag.*, vol. 44 (11), 3307, 2008.

7) **S. Tkachuk**, D. Bowen, I. Nistor, C. Krafft, I. Mayergoyz, "Study of etched (210)-oriented thin garnet films", *J. Appl. Phys.,* vol. 103, 07E503, 2008.

8) I. Nistor, C. Holthaus, **S. Tkachuk**, I. Mayergoyz, C. Krafft, "Magnetic anisotropies in (210)-oriented bismuth substituted iron garnet thin films," *J. Appl. Phys.*, vol. 101, 09C526, 2007.

Introduction

There is no argument that magnets are widely used in modern life. Without solid knowledge about magnetic fields we would not have a lot of the familiar and useful things in our life. Telephones, doorbells, and tape recorders just start the list of the devices where electromagnets are used. Electric motors, generators, and transformers operate using magnetic fields. Modern cars and trains have hundreds of magnetic sensors and electromagnets used for control, safety, and monitoring purposes. Magnetic fields are extensively used for data storage, common television and computer monitors, speakers and microphones, and even in arts and toys. Therefore the measurement and sensing of magnetic fields becomes one of the very important technological tasks. For this reason magnetic field sensors based on Superconducting Quantum Interference Device (SQUID), Hall effect, and Giant magnetoresistance (GMR) effect have been developed and improved.

Quite often not only the field value at a given point is of interest but also the spatial distribution of the magnetic field. Typical examples are visualization of magnetic tracks on audio and video tapes in forensics, security features on banknotes, currents in microelectronic circuits or magnetic fluxes in superconductors. It is also highly desirable for the nondestructive evaluation of material surfaces, where high resolution, two-dimensional, real-time image of the magnetic fields helps one to extract information

about the size and the form of the defect. Imaging of the magnetic fields is based on magnetooptic effects.

In 1845 Michael Faraday discovered that the plane of polarization of linearly polarized light transmitted through glass in a direction parallel to that of an applied magnetic field was rotated. This effect was the first demonstration of the connection between magnetism and light, and the origin of magnetooptics. Since that time, magnetooptics has become a very active field of research, which is of high importance for both the fundamental science as well as applied technology.

Garnet based magnetooptical indicators provide unique capabilities for real time detection and visualization of two-dimensional magnetic field patterns. Their principle of operation is based on the Faraday effect. Bismuth substituted iron garnet thin films are commonly used because of the large Faraday rotation and low absorption in the near infrared region. The quality of garnet based imagers depends on such parameters as sensitivity of the film (amount of rotation per unit of field), dynamic range, and optical losses. Uniformity of the film and absence of defects are also important for the high quality imager. Magnetooptic applications require materials with minimal optical absorption and maximum Faraday rotation. Therefore in order to characterize and compare different materials the magnetooptical figure of merit is introduced, which is defined as the ratio of twice the specific Faraday rotation to the absorption coefficient of the material. Unfortunately it is extremely hard to control these parameters during the garnet film growth process and some of them are mutually exclusive, thus the purpose of

this research is to study properties of the garnet based indicator films in order to increase their performance.

This thesis is structured in the following way. The first chapter explains the basics of the garnet crystals and their properties. The focus of the second chapter is on the film growth and melts design. In order to improve the material properties for specific applications, special experimental techniques are needed to measure them. For this reason the third chapter deals with the characterization of the garnet films. The next chapter describes how the Faraday effect can be enhanced through the use of plasmon resonances. Finally in the last chapter I will report on my work that was done in order to obtain high sensitivity thin garnet film based imagers.

Chapter 1 : Garnet materials and their properties.

Crystal Structure

The garnet group of crystals naturally occurs as nesosilicates and is generally non-magnetic. They have been known for a long time and often used as gemstones and abrasives. The chemical formula of natural garnets is $\{M^{2+}\}_3[M^{3+}]_2(Si^{4+})_3O_{12}$, where $\{M^{2+}\}$-sites are usually occupied by divalent cations (Ca^{2+}, Mg^{2+}, Fe^{2+}) and the $[M^{3+}]$ sites by trivalent cations (Al^{3+}, Fe^{3+}, Cr^{3+}). Garnets have a cubic body centered unit cell with space group O_h^{10} (*Ia3d*) containing 8 formula units.

The chemical formula of the synthetic garnets is $\{RE^{3+}\}_3[Fe^{3+}]_2(Fe^{3+})_3O_{12}$ where rare earth, RE, and iron, Fe, ions fill in three different kinds of interstices between the oxygen ions. Different types of brackets denote three different cation positions. The {RE}-site has 8 oxygen ions as its nearest neighbors located in the corners of a dodecahedron and is called dodecahedral site. The [Fe]-site is octahedral and is surrounded by 6 oxygens. (Fe) indicates a tetrahedral site with four oxygens surrounding it. The crystal structure of yttrium iron garnet is depicted in Fig. 1.1.

For one volume unit (cm^3) of the garnet there are $5.0x10^{22}$ oxygen ions, $2.1x10^{22}$ iron ions, and $1.3x10^{22}$ rare-earth ions. In the iron garnet the $[Fe^{3+}]$ ions have the local point symmetry $\bar{3}$, and the (Fe^{3+}) ions have the local point symmetry $\bar{4}$. The presence of the iron ions in the octahedral and tetrahedral positions gives rise to complicated optical

and magnetooptical spectra as compared, for example, with spectra for orthoferrites [ZveKo97].

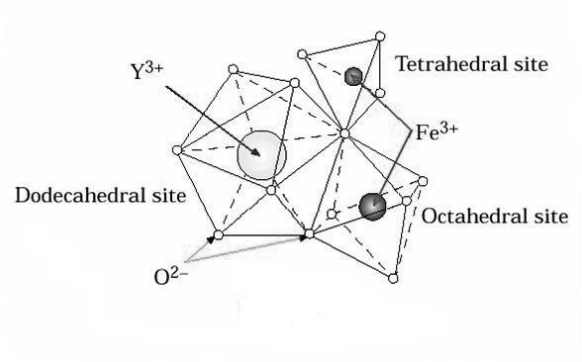

Fig. 1.1. Crystal structure of YIG [www-lar].

Because of the iron ions, synthetic garnets exhibit magnetic behavior. Various magnetic properties can be obtained by substituting specific sites with rare earth and diamagnetic elements. The ferrimagnetic garnets are very useful for practical purposes; for example, they are widely used in developing different magnetooptical devices for optical signal-processing systems and optical communication systems (optical isolators and circulators, switches, time and spatial modulators, sensors, magnetooptical heads and so on). One of the most important properties is magnetization, which we will now consider in more detail.

Magnetization

The ions on the three sites form three magnetically interacting sublattices which tend to orient antiparallel to each other. The main superexchange interaction is an antiferromagnetic one between the octahedral, [Fe^{3+}], and the tetrahedral, (Fe^{3+}) ions. The

next strongest interaction, also antiferromagnetic, is between the tetrahedral, (Fe^{3+}), and the dodecahedral, {RE^{3+}} ions, whereas the weakest interaction is between the dodecahedral, {RE^{3+}}, and the octahedral, [Fe^{3+}] ions. Therefore the sublattice magnetizations orient themselves as in Fig. 1.2. There are also superexchange interactions between the ions belonging to the same sublattice, but such intra-sublattice interactions are only one tenth as strong as the inter-sublattice interactions. The effective magnetic field related to the superexchange between the octahedral and tetrahedral sublattices is nearly 2MOe. The rare-earth ions are in the molecular field formed by the iron ions; the magnitude of such field is of the order of several hundred kOe at room temperature depending on the type of rare-earth ion.

The total magnetization is the algebraic sum of magnetizations of the three sublattices. Contributions from two octahedral ions, $[Fe^{3+}]_2$, and three tetrahedral ions, $(Fe^{3+})_3$, oppose each other, so that their net magnetic moment corresponds to that of one Fe^{3+} . This combined magnetization is aligned antiparallel to the {RE^{3+}}, for the rare earths in the second half of the lanthanide series. Rare-earth ions in the first half of the lanthanide series have their magnetizations aligned parallel to (Fe^{3+}) because they have **J=L-S** rather than **J=L+S** [KaPe69]. The weak coupling between rare earth ions causes the magnetic moment of the dodecahedral sublattice to decrease faster with temperature than that for two iron sublattices, see Fig. 1.2. When the {RE^{3+}} moment becomes equal to the net moment of the octahedral and tetrahedral sublattices, the total magnetization goes through zero and the temperature at which this happens is called the compensation temperature, T_{comp}. All odd magnetooptical effects change their sign when crossing this

point. The Faraday effect changes its sign because above the compensation point magnetization of the tetrahedral lattice orients along the direction of the external magnetic field, while below the compensation point the octahedral lattice orients along the field direction.

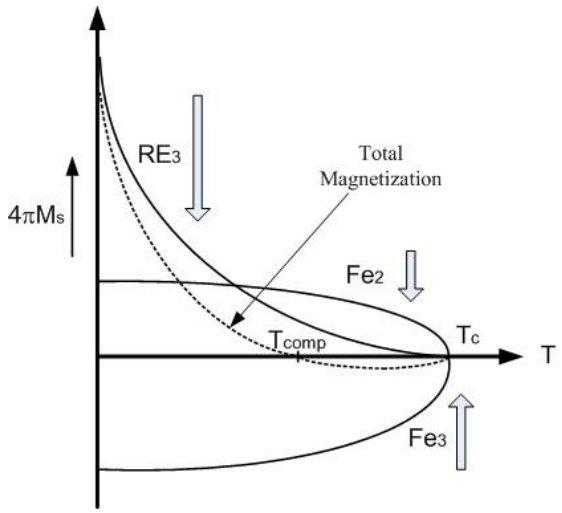

Fig. 1.2. Sublattice magnetization vs. temperature

As the rare-earth sublattice is antiferromagnetically bound to the tetrahedral sublattice, the direction of its magnetization also changes after crossing this point. It is interesting to note that the Curie temperature T_C does not vary much with the type of rare earth element, unlike T_{comp}. This is because T_C is controlled mostly by the strong octahedral/tetrahedral iron interaction. Experimental studies of various rare-earth iron garnets were performed by P. Hansen et al. [HaWi83] and the results for Bi substituted gadolinium iron garnet films are given in the Fig. 1.3.

Garnet magnetization can be precisely controlled by choosing nonmagnetic substituents whose site preference in the garnets is temperature dependent. The most common ions used for this purpose are Ga^{3+} or Al^{3+}. At the usual growth temperature of garnet crystals, about 90% of the gallium goes into tetrahedral sites. By quenching garnets containing Ga^{3+} or Al^{3+} ions at various temperatures the distribution of the nonmagnetic ions on different sites can be changed, which allows precise control of $4\pi M_S$ value [Niel76].

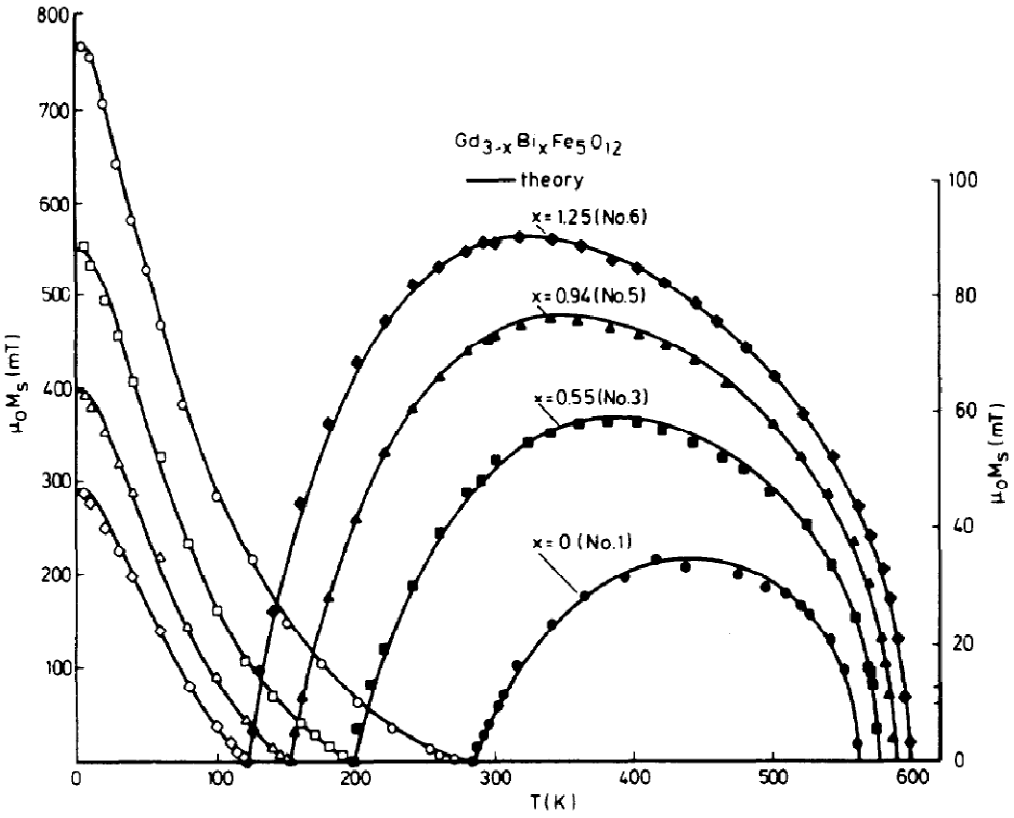

Fig. 1.3. The dependence of the saturation magnetization vs temperature for different Bi content. Theoretical curves were calculated from the molecular field theory. The data for $T < T_{comp}$ (open symbols) apply to the left-hand scale and those for $T > T_{comp}$ (solid symbols) to the right-hand scale [HaWi83].

The dodecahedral sites in garnets can accept several types of atoms at the same time, which allows one to obtain materials with various properties. Magnetic materials that possess two or more inequivalent magnetic sublattices are called ferrimagnetics.

Optical properties

It is well known that iron garnets are highly transparent in the near infrared region (1.5-5.5 μm) of the spectrum (see Fig. 1.4). The optical absorption coefficients of less than 0.03 cm^{-1} in the window range are achieved [WoRe67].

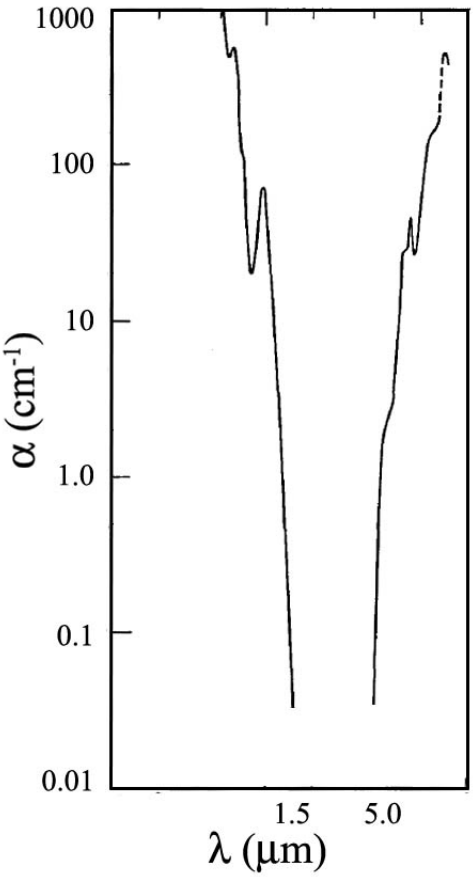

Fig. 1.4. Optical absorption of YIG (based on [WoRe67]).

At a long wavelength side (> 5.5 μm) the large optical absorption is due to vibrations of ions in crystal lattice (phonon absorption). At the other side of the window (wavelength < 1.5 μm) the increase of the optical absorption is related to the intrinsic electron transitions in the trivalent iron ions making up the crystal. There are two causes for the absorption in the lower wavelength range. The first one is due to a charge transfer process; it is very strong and occurs below 0.41 μm. The second one is due to transitions among the levels in octahedral ions of Fe, with the centre of the first absorption band at about 900 nm Fig. 1.5.

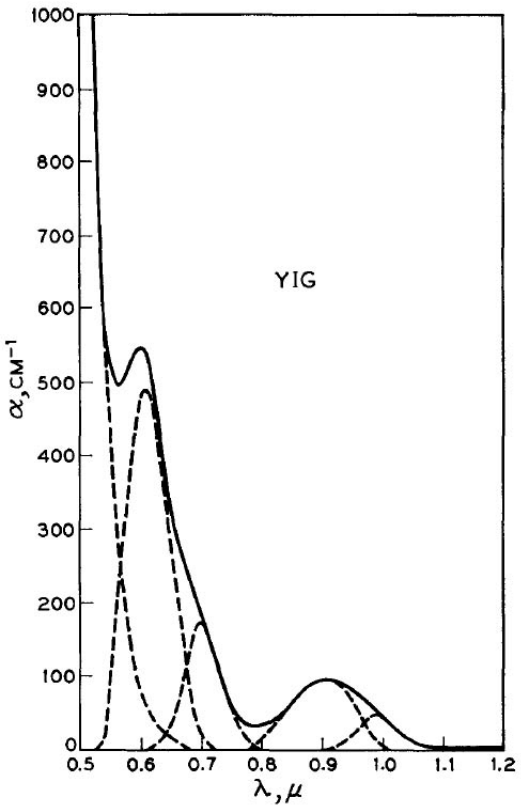

Fig. 1.5. Low wavelength absorption edge of YIG [WoRe67].

Studies of the iron garnet compositions in which the iron sublattice has been diluted with Ga^{3+} have shown [Wem74] that there is a general trend of reduction in the absorption with iron dilution in either the tetrahedral or octahedral sublattices. As has been shown by Hansen and Krumme [HaKru84] the absorption coefficient changes according to

$$\alpha(y) = \alpha_0 \left(1 - \frac{y_a}{2}\right)(1 - \frac{y_d}{3}) \tag{1.1}$$

where y_a and y_d are the contents of diluting ions in the octahedral and tetrahedral positions, and $y = y_a + y_d$.

The presence of the rare-earth ions in the dodecahedral sublattice is exhibited in the appearance of narrow absorption peaks in the transparent band, caused by transitions inside the partially filled 4f shells of the rare-earth ions. Among the trivalent rare-earth ions only La^{3+} and Lu^{3+} ions have no characteristic transitions for the 4f electrons, because lanthanum has no 4f electrons and lutetium has a full 4f shell.

Doping of iron garnets with bismuth greatly increases their magnetooptic activity but is usually accompanied by higher absorption in the visible spectral region. It is rather difficult to determine the contribution of Bi^{3+} ions to the optical absorption because epitaxial growth of films with high bismuth content requires increase of the lead-ion content, which substantially affects the optical absorption. It has been shown [KanOk87] that incorporation of Bi ions up to 1.6 formula units into the iron garnet does not increase optical absorption near λ=0.8 μm if lead ions do not enter the film simultaneously.

Magnetooptical effects

First we will consider main magnetooptical effects in gyrotropic media. In the Faraday effect the angle of rotation of the plane of polarization, θ, is in the simplest case proportional to the magnitude of the magnetic field H and the distance L travelled by light in a medium along the direction of the field:

$$\theta = VHL \tag{1.2}$$

The constant V is called the Verdet constant and has dimensions of degrees of rotation per unit length per unit field strength. It depends on the wavelength of light and properties of the media. The value of the Verdet constant can be found from a well-known Becquerel formula [ZveKo97]:

$$V = \frac{e}{2mc^2}\lambda\frac{dn}{d\lambda} \tag{1.3}$$

where $\lambda = 2\pi c / \omega$ is the wavelength of light and n is the index of refraction.

The sign of the angle θ depends on the sign of the magnetic field H. Thus if the light travels through the media along the direction of the field, gets reflected from a mirror and again travels through the media in the opposite direction, the amount of rotation is doubled. This means that the Faraday effect is a nonreciprocal effect.

The dispersion of the Faraday effect for the $Bi_{1.56}Gd_{1.44}(FeAlGa)_5O_{12}$ film (see Fig. 1.6) along with the dependence of the Faraday rotation on the concentration x of bismuth at wavelength λ=1.3 μm (see Fig. 1.7) was studied by Hibiya et al [Hib85].

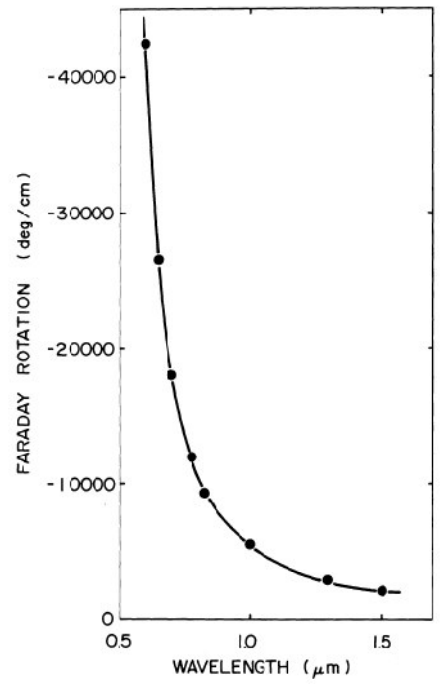

Fig. 1.6. A spectrum of Faraday rotation coefficient.

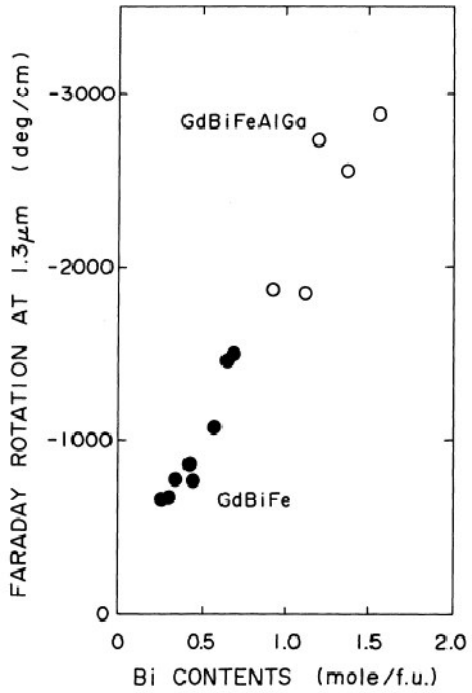

Fig. 1.7. Dependence of Faraday rotation on Bi content.

Optical anisotropy of a magnetized medium also appears when the light is reflected from its surface. Such phenomena are called the magnetooptical Kerr effects (MOKE) and consist in an influence of the magnetization of the medium on the reflected light. It was first discovered by the Scottish physicist John Kerr in 1888. He observed that when linearly polarized light is reflected from the polished pole of an electromagnet, it becomes elliptically polarized with the major axis of the ellipse rotated with respect to the plane of polarization of the incident beam.

Three types of magnetooptical effects in reflection are being distinguished depending on the orientation of the magnetization vector with respect to the surface and the plane of incidence of the light: the polar, longitudinal and transverse Kerr effects. In the polar effect the magnetization vector $\boldsymbol{M}$ is oriented perpendicularly to the reflective surface and in the plane of incidence of the light beam. In the longitudinal effect the magnetization vector $\boldsymbol{M}$ is oriented parallel to the reflective surface and also in the plane of incidence. In the transverse Kerr effect the magnetization $\boldsymbol{M}$ lies in the plane of the surface but perpendicularly to the plane of incidence of the light. The geometries of these effects are shown in Fig. 1.8.

The polar and longitudinal Kerr effects manifest itself in a rotation of the plane of polarization and the appearance of ellipticity of the reflected linearly polarized light due to the magnetization. It is easy to see from the Fig. 1.8 that for both of these effects there is a non-zero projection of the wave vector $\boldsymbol{k}$ of the electromagnetic wave on the magnetization direction $\boldsymbol{M}$. The transverse Kerr effect reveals itself in the change of

intensity and phase of the linearly polarized light reflected from the surface of the magnetized medium. The component of the wave vector along the direction of the magnetization vector is zero.

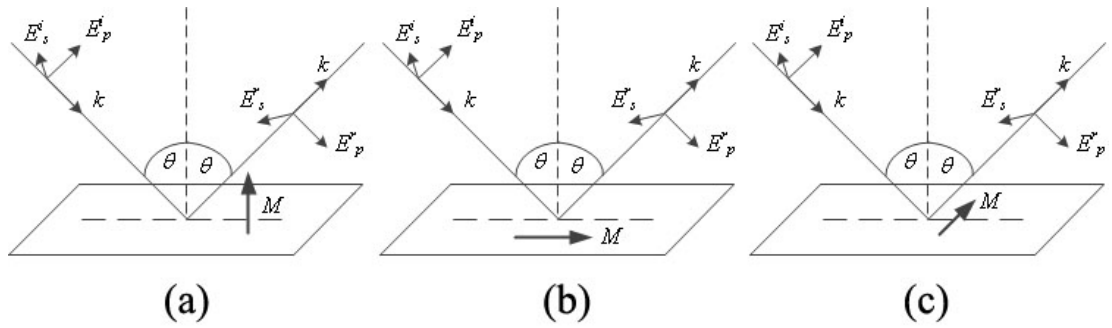

Fig. 1.8. Magnetooptical Kerr effect in (a) polar, (b) longitudinal, and (c) transverse geometries.

The polar Kerr effect is important for optical data storage because it is the basis for reading data from magnetooptical disks. The transverse Kerr effect is particularly useful for observations of magnetic domains at the surface of the magnetized samples. In general the Kerr effects are small, less than a degree in the visible range of the spectrum.

There are multiple other magnetooptical effects such as dichroic photoemission, magnetooptical luminescence, and magnetism-induced second harmonic generation, but we will not consider them and rather focus on the Faraday effect in iron garnet crystals.

Magnetooptical properties of garnets

It is well known that the magnetooptical (MO) effects result from the interaction of electro-magnetic waves with the magnetization in the material. In the macroscopic

theory, all the material properties of garnets are included in a permittivity tensor ε_{ij}, and a magnetic permeability tensor μ_{ij}. It has been shown by Landau and Lifshitz [LaLi84] that the magnetic permeability can be assumed to be unity at optical and near infrared frequencies. Therefore all the MO effects are incorporated in the dielectric permittivity tensor, properties of which will be considered in the following. This tensor can be represented as a sum of two parts, the isotropic, nonmagnetic part and magnetization dependent part:

$$\varepsilon_{ij} = \varepsilon_{ij}^{iso} + \Delta\varepsilon_{ij}(\vec{M}) \tag{1.4}$$

The isotropic part can be assumed to have the following form:

$$\varepsilon_{ij}^{iso} = \begin{pmatrix} \varepsilon_d & 0 & 0 \\ 0 & \varepsilon_d & 0 \\ 0 & 0 & \varepsilon_d \end{pmatrix} \tag{1.5}$$

The magnetization dependent part $\Delta\varepsilon_{ij}(\vec{M})$, for all practical cases, can be expanded in power series of $\vec{M}$ [Wet76]

$$\Delta\varepsilon_{ij}(\vec{M}) = \sum_{k=1}^{3} K_{ijk} M_k + \sum_{k=1}^{3}\sum_{l=1}^{3} G_{ijkl} M_k M_l + \cdots \tag{1.6}$$

where K_{ijk} and G_{ijkl} are the components of the linear and quadratic magneto-optical tensor, respectively. Neglecting the quadratic term and using symmetry of the cubic crystal along with Onsager relation $\varepsilon_{ij}(\vec{M}) = \varepsilon_{ji}(-\vec{M})$, one can find nonzero components of tensor K_{ijk} :

$$K_{123} = K_{231} = K_{312} = -K_{213} = -K_{321} = -K_{132} = K. \tag{1.7}$$

All other components vanish.

Consider now a plane wave $\vec{E} = \overrightarrow{E_0} e^{i(\omega t - kz)}$ propagating perpendicular to the film plane with wave vector $\vec{k} = (0,0,k)$. We will assume out-of-plane magnetization with $\vec{M} = M_s(0,0,1)$. The permittivity tensor can be written as

$$\varepsilon_{ij} = \begin{pmatrix} \varepsilon_d & KM_s & 0 \\ -KM_s & \varepsilon_d & 0 \\ 0 & 0 & \varepsilon_d \end{pmatrix} \tag{1.8}$$

With the assumption that there are no free charges and that the material is a linear dielectric, Maxwell's equations reduce to the well known wave equation for $\vec{E}$,

$$\nabla^2 \vec{\mathrm{E}} - \frac{1}{\mathrm{c}^2} \hat{\varepsilon} \frac{\partial^2 \vec{\mathrm{E}}}{\partial \mathrm{t}^2} = 0 \tag{1.9}$$

In the geometry of interest, the Laplacian simplifies to $d^2\vec{E}/dz^2$, which along with the tensor (1.8) allows us to write

$$\frac{d^2}{dz^2} \begin{bmatrix} E_x \\ E_y \\ 0 \end{bmatrix} + \frac{\omega^2}{c^2} \begin{bmatrix} \varepsilon_d & KM_s & 0 \\ -KM_s & \varepsilon_d & 0 \\ 0 & 0 & \varepsilon_d \end{bmatrix} \begin{bmatrix} E_x \\ E_y \\ 0 \end{bmatrix} = 0 \tag{1.10}$$

For a clockwise polarized wave, the field has the form

$$\overrightarrow{E^{cw}} = E^{cw}(\hat{x} - j\hat{y}) \tag{1.11}$$

Substituting (1.11) into (1.10) we get the propagation constant

$$k^{cw} = \frac{\omega}{c}(\varepsilon_d - jKM_s)^{1/2} = k_0(\varepsilon_d - jKM_s)^{1/2} = k_0 n_- \tag{1.12}$$

Similarly for the counterclockwise wave $\overrightarrow{E^{ccw}} = E^{ccw}(\hat{x} + j\hat{y})$ the propagation constant can be found as $k^{ccw} = k_0(\varepsilon_d + jKM_s)^{1/2} = k_0 n_+$.

The difference in the propagation velocities of the right and left circular polarized waves causes rotation of the plane of polarization, which is called magnetic circular birefringence (MCB). To illustrate this let's look at a linearly polarized wave propagating in the +z direction with $\vec{E}$ field vector in the $\hat{x}$ direction. This field may be decomposed into circularly polarized modes of propagation

$$\overrightarrow{E^{cw}} = (\hat{x} - j\hat{y})\frac{E}{2}e^{-jk^{cw}z}, \text{ and } \overrightarrow{E^{ccw}} = (\hat{x} + j\hat{y})\frac{E}{2}e^{-jk^{ccw}z} \tag{1.13}$$

since their sum at $z = 0$ is $\vec{E} = \hat{x}E$. The field at some other plane $z = d$ can be found as

$$\vec{E} = Ee^{-\left(\frac{j}{2}\right)(k^{cw}+k^{ccw})d}\left[\hat{x}\cos\left(\frac{k^{cw}-k^{ccw}}{2}\right)d - \hat{y}\sin\left(\frac{k^{cw}-k^{ccw}}{2}\right)d\right] \tag{1.14}$$

By introducing the following equalities

$$\begin{aligned} \frac{k^{cw}+k^{ccw}}{2} &= k_0 n_0 = k_0(n_0' + jn_0''), \text{ and} \\ \frac{k^{cw}-k^{ccw}}{2} &= k_0\Delta n = k_0(\Delta n' + j\Delta n''), \end{aligned} \tag{1.15}$$

eqn. (1.14) can be written as

$$\vec{E} = Ee^{-jk_0n_0d}\begin{bmatrix}\cos\left(k_0d(\Delta n' + j\Delta n'')\right)\\ -\sin\left(k_0d(\Delta n' + j\Delta n'')\right)\end{bmatrix}$$

$$= Ee^{-jk_0n_0d}\begin{bmatrix}\cos(k_0\Delta n'd)\cosh(k_0\Delta n''d) - j\sin(k_0\Delta n'd)\sinh(k_0\Delta n''d)\\ -\sin(k_0\Delta n'd)\cosh(k_0\Delta n''d) - j\cos(k_0\Delta n'd)\sinh(k_0\Delta n''d)\end{bmatrix} \quad (1.16)$$

The angle between directions of the vector $\vec{E}$ at $z = 0$ and $z = d$ is called Faraday rotation angle and can be found simply as $tan(\theta_F) = \tan(k_0\Delta n'd)$, and therefore

$$\theta_F = k_0\Delta n'd \quad (1.17)$$

In general, the clockwise (-) and counterclockwise (+) components of the electromagnetic wave will also have different absorption coefficients, $\alpha_{\mp}$. Writing $\vec{E}$ as a linear combination of these components (1.13), and reorganizing the terms, we have

$$\vec{E} = \frac{E}{2}e^{-jk_0n_0z}[\hat{x} + j\hat{y}]e^{jk_0\Delta nz} + \frac{E}{2}e^{-jk_0n_0z}[\hat{x} - j\hat{y}]e^{-jk_0\Delta nz} \quad (1.18)$$

Substituting n_0 and Δn as a sum of real and imaginary parts, similarly to (1.15), we obtain the following equation

$$\vec{E} = \frac{E}{2}e^{k_0(n_0'' - \Delta n'')z}[\hat{x} + j\hat{y}]e^{-jk_0(n_0' - \Delta n')z} \quad (1.19)$$

$$+ \frac{E}{2}e^{k_0(n_0'' + \Delta n'')z}[\hat{x} - j\hat{y}]e^{-jk_0(n_0' + \Delta n')z}$$

Thus, for the clockwise and counterclockwise polarized waves, by inspection, $-\alpha_{\mp}z/2 = k_0(n_0'' \pm \Delta n'')z$, or

$$\alpha_{\mp} = -2k_0(n_0'' \mp \Delta n'') \tag{1.20}$$

The difference between the absorption coefficients is called magnetic circular dichroism (MCD).

Microscopic theory of Faraday Effect

The understanding of the microscopic mechanisms of the magneto-optic effects is based on the knowledge of the electronic structure and electron wave functions in crystals. Particularly important are the selection rules for light-induced quantum transitions. It is well known that right or left circularly polarized light excites electron transitions that change the projection of the system's angular momentum by $\Delta m = \pm 1$. The Faraday and Kerr effects are defined by the difference between the contributions of the transitions with $\Delta m = +1$ and $\Delta m = -1$.

In the microscopic theory of the magneto-optic effects, the dielectric susceptibility tensor ε_{ij} is replaced by its quantum mechanical expression. Following the discussion by Frederic Kahn et al. [Kahn69] magneto-optic effects result from the splitting of the ground or excited state energy levels of optical transitions due to an applied field or a magnetization. In the axial magneto-optic effects, magnetic circular birefringence (Faraday rotation) and magnetic circular dichroism (Faraday ellipticity), a difference in the optical constants strongly affects right and left circularly polarized waves. Without applied magnetic field $\boldsymbol{H}$ or magnetization $\boldsymbol{M}$ this difference would be zero.

For the optical transitions of the octahedral FeO_6^{9-} and tetrahedral FeO_4^{5-} complexes the following statements can be made:

1. The transitions exhibit mainly electric dipole character. Magnetic dipole transitions are an order of magnitude weaker to explain the experimental spectra.
2. The ground state is a singlet, only the lowest of the exchange split levels of the ^6S ground state is thermally occupied at room temperature.
3. Magneto-optic effects arise from splitting of the excited states by a combined effect of spin-orbit coupling and exchange.
4. The direct effect of the applied magnetic field $\boldsymbol{H}$ on the orbitals (Zeeman effect) can be neglected compared to the effect of exchange and spin-orbit coupling.

The off-diagonal tensor element $\Delta\varepsilon_{12}$, which is responsible for the Faraday rotation and Faraday ellipticity, can be expressed in terms of the difference of right and left circularly polarized transition matrix elements. An electric dipole transition between a ground state |g> and excited state |e(v)> can be expressed as

$$\Delta\varepsilon_{12} = \frac{2\pi N e^2}{m} \sum_{e,v} \frac{f_{+e(v)} - f_{-e(v)}}{\omega^2 - \omega_{e(v)}^2 - \Gamma_{\mathrm{e(v)}}^2 - 2i\Gamma_{\mathrm{e(v)}}} \cdot \frac{\omega - i\Gamma_{\mathrm{e(v)}}}{\omega_{e(v)}}. \tag{1.21}$$

Here $f_{\pm e(v)}$ are the oscillator strengths for right and left circularly polarized transitions, respectively, N is the number of spins, e and m are electron charge and mass, $\omega_{e(v)}$ is the transition frequency to the excited level |e(v)> where v is the number of sublevels due to spin-orbit coupling and exchange.

The main contribution to the Faraday rotation effect comes from the splitting of the excited states due to spin-orbit coupling. In magnetic crystals, the exchange splitting is much larger than the Zeeman splitting of the energy levels. However, the exchange acts only on the spins, not on the orbitals and, therefore, cannot give rise to the magneto-optic effects. It is only the spin-orbit coupling that allows the orbitals to sense the polarization of light via the selection rules.

The spin-orbit coupling can, to first order in $\boldsymbol{M}$, either split the excited state |e> and leave the oscillator strengths $f_{\pm e(v)}$ of the sublevels approximately unchanged (case I) or leave the excited state degenerate and split the oscillator strengths (case II). For these two cases the dispersion relation of the $\Delta\varepsilon_{12}$ shows different behavior. This difference in the dispersion behavior can be a useful tool for investigating the structure of optical transitions in magnetic crystals. It is important to mention that the transitions considered above are the dominant contributions to the Faraday rotation in the visible spectral range. In the infrared region the low frequency ferromagnetic resonance should be taken into account as well.

The Faraday effect and magnetic susceptibility of the rare-earth garnets over wide wavelength and temperature ranges were extensively studied by Valiev et al [Val90]. The results of their measurements were processed in order to obtain the Verdet constant, which can be written as

$$V = -\frac{\omega^2}{\omega_0^2 - \omega^2}\left[\frac{2\omega_0 A}{\hbar(\omega_0^2 - \omega^2)} + B + C\chi\right] + V_{gm} \tag{1.22}$$

where χ is the paramagnetic susceptibility of a rare-earth subsystem, ω_0 is the effective transition frequency, and V_{gm} is the gyromagnetic contribution to the Verdet constant. The constants A, B, and C are fitting constants that depend on the types of rare-earth contained in garnet samples.

For the bismuth substituted rare earth iron garnets the large increase in the Faraday rotation Verdet constant is caused by the increase of the spin-orbit interaction due to the formation of the molecular orbit between 3*d* orbital in Fe^{3+} and 2*p* orbital in O^{2-} mixed with 6*p* orbital in Bi^{3+} having a large spin-orbit interaction coefficient.

Magnetic free energy density

The ions in the garnet film all have spins and magnetic moments and are involved in different interactions. Each interaction gives a contribution to the magnetic free energy density. The first one is due to the atoms interacting with each other, and is described by the exchange energy density, E_{exch}. The second contribution is determined by the film shape, and results in a demagnetization energy density, E_{dem}. The anisotropy energy density, E_K, combines the cubic or crystalline anisotropy energy, E_C, and growth induced anisotropy energy, E_G. Often the magnetoelastic energy density, E_S, is also included in this term. The crystalline anisotropy is due to the cubic structure of the garnet crystal, the growth anisotropy energy is induced by the peculiarities of the film growth process, and the magnetoelastic component originates in local stress related to the mismatch between substrate and film lattices. Finally if an external magnetic field is applied, there will be magnetic field energy density term which is often called Zeeman energy, and describes

the interaction between the applied field and the magnetization vector. Let's consider each of the above mentioned contributions in detail.

The exchange energy is of a quantum mechanical origin, and for a pair of nearest neighbor spins S_i and S_j can be expressed in the form

$$\varepsilon_{ij} = -2J\overrightarrow{S_i} \cdot \overrightarrow{S_j} \tag{1.23}$$

where J is the exchange integral. For $J > 0$, the lowest energy is attained when the two spins are parallel to each other. A network of spins, therefore, tends to be aligned. At 0 K the net magnetic moment per unit volume has the largest value, and reduces as the temperature increases due to the misalignment of the spins caused by thermal agitation. The temperature at which all the long-range alignment is completely disrupted and the magnetization reaches zero is called the Curie temperature, T_C.

For a network of spins we can sum up the exchange energies for each pair to obtain an exchange energy density. For a cubic lattice with spacing, a, it takes the following form

$$E_{exch} = A\sum_{i=1}^{3}(\nabla\alpha_i)^2 \tag{1.24}$$

where $A = 2JS^2/a$ and α_1, α_2, α_3 are the direction cosines of the orientation of the local magnetization.

If a magnetic body of finite size is magnetized, free magnetic poles are induced on both its ends. These, in turn, give rise to a magnetic field in a direction opposite that of magnetization. This field, called the demagnetizing field, H_{dem}, can be described by the demagnetization tensor $\hat{N}$:

$$\vec{H}_{dem} = -\hat{N}\vec{M} \tag{1.25}$$

The corresponding energy density can be written as

$$E_{dem} = -{}^{1}/_{2}\,\vec{M}\vec{H}_{dem} \tag{1.26}$$

In the principal axis system of an ellipsoid the demagnetization tensor has diagonal form

$$\hat{N} = \begin{pmatrix} N_x & 0 & 0 \\ 0 & N_y & 0 \\ 0 & 0 & N_z \end{pmatrix} \tag{1.27}$$

where the components are related by

$$N_x + N_y + N_z = 4\pi \tag{1.28}$$

For a thin garnet film, only N_z is non zero, therefore the demagnetizing field is

$$\vec{H}_{dem} = -N_z M_z = -N_z M cos\theta \tag{1.29}$$

where θ is the angle between vector of magnetization and the film normal.

Combining (1.26), (1.28) and (1.29) we obtain for the demagnetizing energy density:

$$E_{dem} = -{}^{1}/_{2}\,\vec{M}\vec{H}_{dem} = 2\pi M^2 cos^2\theta \tag{1.30}$$

The demagnetization energy is reduced by the formation of domains of reversed magnetization and approaches zero as the net magnetization goes down.

The anisotropy energy is related to the orientation of the magnetization with respect to some internal structure of the film. In garnet crystals the magnetization is oriented spontaneously into "easy" directions, whereas some energy must be spent to rotate it into a "hard" direction.

Since the garnets are cubic materials, the expression for the crystalline anisotropy energy density reflects that cubic symmetry:

$$E_C = K_1(\alpha_1^2\alpha_2^2 + \alpha_2^2\alpha_3^2 + \alpha_3^2\alpha_1^2) + K_2\alpha_1^2\alpha_2^2\alpha_3^2 + \cdots \tag{1.31}$$

where the α's are the direction cosines of the magnetization, and K's are the cubic anisotropy constants. In the following we will neglect the higher orders and use only K_1.

The growth induced anisotropy is primarily produced by the preferential distribution of rare earth ions on certain lattice sites depending on the growth orientation, the deposition parameters and the identity of the ions. For the cubic crystalline films the growth-induced anisotropy can be expressed as

$$E_G = A(\alpha_1^2\beta_1^2 + \alpha_2^2\beta_2^2 + \alpha_3^2\beta_3^2) + B(\alpha_1\alpha_2\beta_1\beta_2 + \alpha_2\alpha_3\beta_2\beta_3 + \alpha_1\alpha_3\beta_1\beta_3), \tag{1.32}$$

where β_1, β_2, β_3 are the direction cosines of the film growth direction.

Magnetoelastic energy density originates from the mechanical stress due to the mismatch between the substrate lattice and the film lattice spacing, $\Delta a_0 = a_0^s - a_0^f$. It is given by the following expression

$$E_S = \frac{3}{2}\lambda_{100}\sigma_0(\alpha_1^2\beta_1^2 + \alpha_2^2\beta_2^2 + \alpha_3^2\beta_3^2) \tag{1.33}$$

$$+3\lambda_{111}\sigma_0(\alpha_1\alpha_2\beta_1\beta_2 + \alpha_2\alpha_3\beta_2\beta_3 + \alpha_1\alpha_3\beta_1\beta_3),$$

where λ_{100} and λ_{100} are the magnetostrictive coefficients of the film material. The stress can be related to the mismatch in lattice spacing by the following formula

$$\sigma_0 = \frac{E}{1-\nu}\frac{\Delta a_0}{a_0}, \tag{1.34}$$

where E is Young's modulus and ν is Poisson's ratio. Comparing the demagnetizing energy density with the magnetoelastic energy, it can be verified that when $4\pi M_S$ is smaller than a few hundred gauss, the lattice mismatch can be sufficient to orient the magnetization perpendicular to the film.

Now, after considering the main optical, magnetic and magneto-optical properties of garnets, we can take a look at the melt design and film growth process.

Chapter Bibliography

[HaKru84] P. Hansen and J. P. Krumme, "Magnetic and magneto-optical properties of garnet films", *Thin Solid Films*, **114**, 69 (1984).

[HaWi83] P. Hansen, K. Witter, and W. Tolksdorf, "Magnetic and Magneto-optical properties of bismuth-substituted gadolinium iron garnet films", *Phys. Rev. B.*, **27**, 4375 (1983).

[Hib85] T. Hibiya, Y. Morishige, J. Nakashima, "Growth and characterization of Liquid-phase epitaxial Bi-substituted iron garnet films for magneto-optic applications", *Japan. J. Appl. Phys.*, **24**, 1316 (1985).

[Kahn69] F. J. Kahn, P. S. Pershan, and J. P. Remeika, "Ultraviolet Magneto-Optical Properties of Single-Crystal Orthoferrites, Garnets, and other Ferric Oxide Compounds", *Phys.Rev.*, **186** (2), 891 (1969).

[KanOk87] M. Kaneko, T. Okamoto, H. Tamada and K. Sako," A low-loss 0.8-mum band optical isolator using highly Bi-substituted LPE garnet film", *IEEE Trans. Magn.*, 23, 3482 (1987).

[KaPe69] F.J. Kahn, P.S. Pershan, and J.P. Remeika, "Ultraviolet Magneto-Optical Properties of Single-Crystal Orthoferrites, Garnets, and Other Ferric Oxide Compounds", *Physical Review*, **186**, p.891 (1969).

[LaLi84] L.D. Landau and E.M. Lifshitz, "Electrodynamics of continuous media", *Pergamon Press*, New York, 1984.

[Niel76] J. W. Nielsen, "Bubble Domain Memory Materials", *IEEE Trans. Mag.*, **12**, 327 (1976).

[Val90] K. M. Mukimov, B. Y. Sokolov, U.V. Valiev, "The Faraday Effect of rare-earth ions in garnets", *Physica Status Solidi A-Applied Research*, **119**, 307 (1990).

[Wem74] S. H. Wemple, S. L. Blank and J. A. Seman, "Optical properties of epitaxial iron-garnet thin films", *Phys. Rev. B*, **9**, 2134 (1974).

[Wet76] W. Wettling, "Magneto-optics of ferrites", *Journal of Magnetism and Magnetic Materials*, **3**, pp.147-160 (1976).

[WoRe67] D. L. Wood and J. P. Remeika, "Effect of impurities on the optical properties of yttrium iron garnet", *Jour. Appl. Phys.*, **38**, 1038 (1967).

[www-lar] http://www.larsenglish.com/magneticresonance

[ZveKo97] A. K. Zvezdin and V. A. Kotov, "Modern Magnetooptics and Magnetooptical Materials", *Institute of Physics Publishing*, Bristol and Philadelphia, p. 163, 1997.

Chapter 2 : Film growth and melt design

The development of the MO imager is comprised of several major steps where each of them includes many elementary processes. The major steps are: growth of the properly oriented nonmagnetic garnet crystal boule, preparation of the substrates, and finally deposition of the magnetic films on the substrates.

The substrates must be nonmagnetic, single crystal, rigid, flat and with smooth surfaces. They should have no defects and lattice spacing, a_0, should be appropriate for the desired film to be grown. The usual choice of material for substrates is gadolinium gallium garnet (GGG), where Ga substitutes for Fe which leads to substrate being nonmagnetic. The regular GGG substrate has a lattice constant a_0 = 1.2384 nm which is close to the lattice constant of pure YIG, a_0 = 1.2374 nm. In case the desired film has larger ions such as Bi or Pr, the modified substrates with extended lattice spacing need to be used. These substrates can be obtained by addition of calcium, magnesium and zirconium ions during the boule growth which is done by the Czochralski method. Such substitutions allow obtaining substrates with lattice constant in a range from 1.2382 nm to 1.2511 nm [MaRu77].

Liquid phase epitaxy growth

Since the rare-earth iron garnets are not congruently melting compounds their growth by the Czochralski method is not possible. The alternative growth methods have been developed such as liquid phase epitaxy, chemical vapor deposition (CVD) [RoBo71], pulsed laser deposition [DoBu93], and RF-sputtering. For the purpose of MO

imager development the preferred approach of garnet film growth is the dipping liquid phase epitaxy (LPE) technique. This method has high deposition rate on the order of μm/min, yields films of high crystalline quality, and gives possibility of controlling the material properties of the sample. The essence of the method is dipping of the substrate into a supersaturated flux solution containing garnet. A schematic representation of the LPE-furnace used for garnet growth is shown in Fig. 2.1. An image of the actual LPE growth system developed at Laboratory for Physical Sciences is presented in Fig. 2.2.

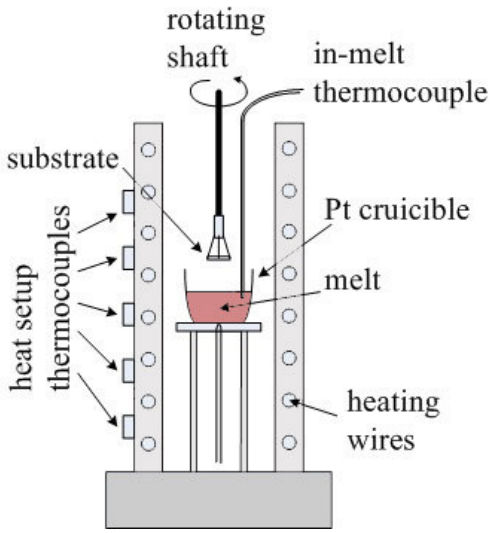

Fig. 2.1. Sketch of LPE-furnace.

A platinum crucible, filled with appropriate amounts of oxides that are premixed, is placed in the furnace. Platinum has to be used because of its high melting point and resistivity against the corrosive melt. The furnace is heated up for several hours to a temperature above the saturation temperature for the oxide mixture and the melt is

homogenized by stirring it with a platinum stirrer for about 30 minutes. After that the melt is set to cool down to the growth temperature and the substrate is prepared for growth. Before the growth process, a garnet substrate of specific crystallographic orientation is cleaned with acetone and ethyl alcohol, rinsed in deionized water and etched in hot (approximately 120°C) phosphoric acid to remove any impurities from its surface. Then it is placed horizontally into the platinum substrate holder, attached to a long rod, and slowly lowered in the furnace to allow equilibrium and avoid thermal shock. The grown sample might have transition layers caused by different growth conditions at a cold substrate if not enough time is given to match the temperatures of substrate and melt. When melt and substrate reach the growth temperature, the substrate is lowered into the undercooled melt and just as it touches the melt surface, is pulled up a short distance, keeping contact with the melt through the meniscus which is formed. This allows film growth only on one side of the substrate to simplify characterization. The immersed substrate is rotated axially at a constant frequency (in a range from 64 to 196 rpm). The speed of rotation affects growth rate of the sample and therefore its properties. Typical growth rates for my melt compositions and growth conditions are within 0.2-0.9 μm/min. The growth time depends on the desired thickness of the sample and is easy to estimate if approximate growth rate is known for the given melt and growth conditions. When the growth time has elapsed the sample is removed from the melt and the speed of rotation is increased to 400 rpm in order to spin off the remnants of the flux. Then it is slowly moved out of the furnace because the crystal will crack if removed too fast. Finally the sample is cleaned in a hot (about 90°C) solution of nitric acid (10%), acetic

acid (10%), and water (80%). If the same melt is used for the next growth process it should be again brought above the melting point and homogenized by stirring.

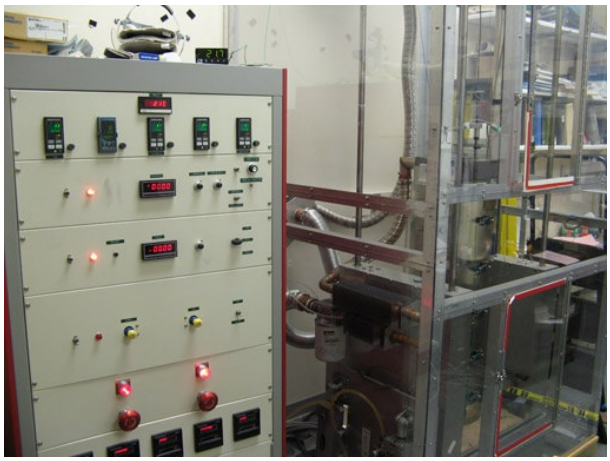

Fig. 2.2. LPE garnet growth apparatus.

The proper design of the melt used in LPE growth of thin garnet films is extremely important in order to be able to obtain the samples with the desired characteristics.

Melt Engineering

The melt contains a mixture of appropriate oxides of the rare-earths, iron and iron dilutants such as Ga or Al, along with lead oxide (PbO) and boron oxide (B_2O_3) flux. Bismuth oxide is part of flux and garnet phases. The quantity of each oxide composing a melt needs to be carefully calculated and precisely weighed since not only do the properties of the garnet film depend on it but even the possibility to obtain garnet itself can be lost. To illustrate the point we can consider pseudo-ternary mixture PbO-Y_2O_3-

Fe_2O_3 (see Fig. 2.3) [Niel58]. It can be seen that depending upon where the overall composition lies, one of four primary phases, hematite (Fe_2O_3), magnetoplumbite ($PbFe_{12}O_{19}$), garnet ($RE_3Fe_5O_{12}$) or orthoferrite ($REFeO_3$) will crystallize. The usual garnet has more constituents than represented in the simpler system of Fig. 2.3, but it can be helpful to think of the complex garnet as a pseudo-ternary: flux-$\sum RE_2O_3$-$\sum Fe_2O_3$, Ga_2O_3.

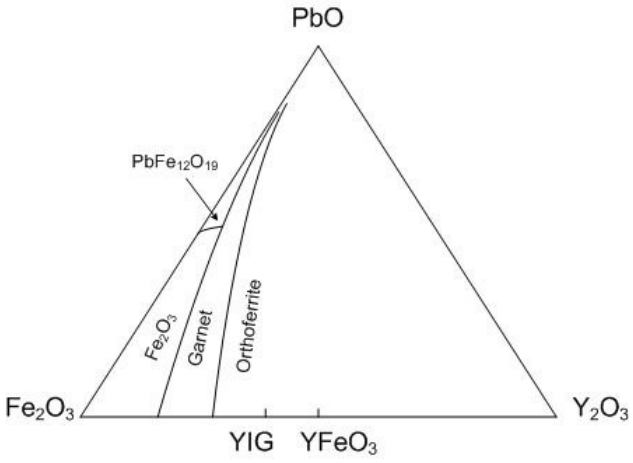

Fig. 2.3. Pseudoternary PbO-Fe2O3-Y2O3 phase equilibrium diagram showing magnetoplumbite, hematite, garnet and orthoferrite primary phase fields.

The following system of cation ratios was introduced for describing the composition of a garnet melt [BlaN72]. The ratio of iron oxide and its substituents to rare earth oxides is given as R_1. This ratio is generally much higher than the stoichiometric value 5:3 and ranges anywhere from 7.5 to 17.5. Increasing R_1 decreases the saturation temperature of the melt and increases Bi incorporation. The ratio of the sum of the garnet-forming oxides to the sum of the flux oxides describes the concentration of garnet

oxides in the melt and is referred to as *G*/*F*. This ratio also controls the saturation temperature of the melt and the growth rate, and varies from 0.12 to 0.2. The concentration of Bi in the melt is given by the ratio of bismuth to the sum of lead and bismuth and is denoted by C_{Bi}. It controls the Bi incorporation and can be anywhere between 0.2-0.8. The boron concentration, C_{B}, is similarly the ratio of boron to the sum of lead and bismuth. Addition of boron oxide to the melt has very strong effect on the saturation temperature; it stabilizes the melt allowing for larger undercooling but also increases viscosity of the melt. C_{B} should be kept within 0-0.25. The ratio of iron to its substituents, R_2, controls diamagnetic substitutions and affects the $4\pi M_{\mathrm{S}}$ value. The equations for these parameters are given below:

$$\frac{G}{F} = \frac{\sum RE + [Fe] + [Ga] + [Al]}{[Pb] + [Bi] + [B]}, \tag{2.1}$$

$$C_{Bi} = \frac{[Bi]}{[Pb] + [Bi]}, \tag{2.2}$$

$$C_B = \frac{[B]}{[Pb] + [Bi]}, \tag{2.3}$$

$$R_1 = \frac{[Fe] + [Ga] + [Al]}{\sum RE}, \tag{2.4}$$

$$R_2 = \frac{[Fe]}{[Ga] + [Al]}. \tag{2.5}$$

The square brackets in these expressions denote the corresponding cations with no charge or oxygen coordination shown. To determine the masses of the necessary oxides for the

mixture, the cation percentages of each element need to be calculated from the cation ratios. Using the cation ratios and the stoichiometric formulas for each oxide the molar percentages should be found. Based on the molar percentages and the molar mass of each oxide the amount of each component can be obtained in grams.

There are several phenomena that must be well understood and controlled in order to grow high quality garnet films by liquid phase epitaxy technique: phase equilibrium in a fluxed melt of garnet, epitaxial crystallization from a super cooled melt, boundary layer depletion and replenishment, and film/melt segregation. The garnet crystallization from the melt occurs at the melt/substrate interface, and therefore a concentration of the garnet constituents close to the surface of the melt will be decreasing. This will cause depletion of the melt surface and create a gradient in the garnet concentration. Diffusion caused by the concentration gradient will replenish the melt surface and allow for the further crystal growth. The balance between the melt depletion and replenishment determines the growth rate. It can be increased by introducing a convective flow produced by rotation of the substrate at an angular rate ω. The experimental data [Esch81] demonstrate that the growth rate dependence on rotation rate is close to $\omega^{1/2}$ while dependence on the undercooling, ΔT, and the concentration of garnet constituents, C, is approximately linear:

$$growth\ rate \propto C\Delta T\omega^{1/2}, \tag{2.6}$$

In this chapter I have discussed the film growth process and the principles of melt design. The LPE technique is used because it allows for the growth of relatively thick

single crystal garnet films with controllable properties. These properties depend on the composition of the film as well as the type of the substrate. The film composition, in turn depends on the growth rate and the composition of the melt. In the next chapter I will consider the standard techniques for characterization of the garnet film properties.

Chapter Bibliography

[BlaN72] S.L. Blank, J.W. Nielsen, "Growth of magnetic garnets by liquid-phase epitaxy", *Journal of Crystal Growth*, **17**, 302 (1972).

[DoBu93] P.C. Dorsey, S.E. Bushnell, R.G. Seed, and C. Vittoria, "Epitaxial yttrium iron garnet films growth by pulsed laser deposition", *Journal of Applied Physics*, **74**, 1242 (1993).

[Esch81] A.H. Eschenfelder, "Magnetic Bubble Technology", *Springer-Verlag*, New York (1981).

[Frat89] V. J. Fratello, S.J. Licht, and M.P. Norelli, "Effect of melt composition on Bi incorporation in iron garnets", *Journal of Crystal Growth*, **97**, 657 (1989).

[MaRu77] D. Mateika, and C. Rusche, "Coupled substitution of gallium by magnesium and zirconium in single crystals of gadolinium gallium garnet", *Journal of Crystal Growth*, **42**, 440 (1977).

[Niel58] J. W. Nielsen, E. F. Dearborn, "The growth of single crystals of magnetic garnets", *Journal of Physics and Chemistry of Solids*, **5**, 202 (1958).

[RoBo71] M. Robinson, A.H. Bobeck, and J.W. Nielsen, "Chemical Vapor Deposition of Magnetic Garnets for Bubble-Domain Devices", *IEEE Transactions on Magnetics*, **7**, 464 (1971).

Chapter 3 : Characterization of the garnet films

Lattice mismatch measurement

Generally the lattice constants of the film (a_f) and the substrate (a_s) will not match exactly, thus an important parameter can be introduced

$$\Delta a = a_s - a_f, \tag{3.1}$$

which is called *lattice mismatch*. The film can grow on the substrate as a single crystal only if this mismatch is sufficiently small [Hol04], -0.07Å< Δa < 0.03Å. Since the thickness of the substrate is significantly larger than that of the grown film, its lattice constant will remain the same, whereas the crystal lattice of the film will elastically deform to match its lattice constant to the substrate along the interface. This deformation has to be compensated in the direction perpendicular to the interface and the lattice structure of the film becomes noncubic. Such mismatch in perpendicular lattice spacing of the film and the substrate can be measured by x-ray diffraction. If the lattice constant of the film is larger than the lattice constant of the substrate ($\Delta a<0$) then the film is under compression, in the opposite case ($\Delta a>0$), the film is under tension (see Fig. 3.1). The perpendicular component of lattice spacing is measured with x-ray diffractometer, where a beam is reflected off a GaAs crystal under (400) direction. A detector and the sample are moved in such a way that the angle between the sample surface and the incident beam is always θ whereas the angle between the detector and the beam is always 2θ. The x-ray source emits CuK$\alpha_{1,2}$ lines with wavelengths $\lambda_{\alpha 1}$=0.15405 nm and $\lambda_{\alpha 2}$=0.15444 nm.

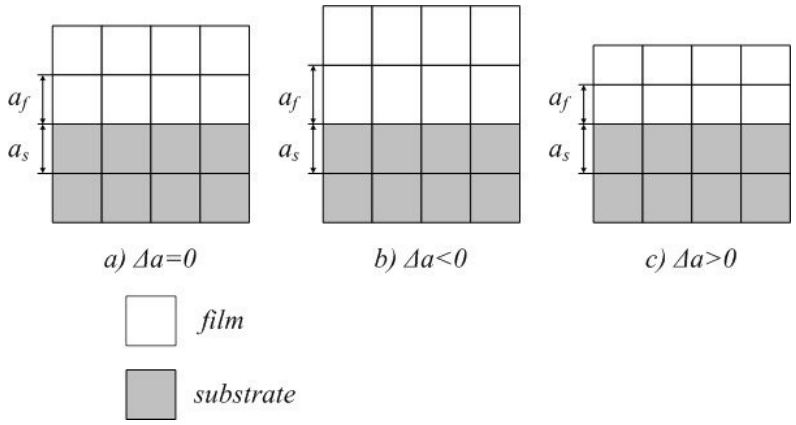

Fig. 3.1. Lattice mismatch between garnet film and substrate: a) no mismatch, b) film under compression, c) film under tension.

The signal of the scintillation counter depends on the incidence angle θ and has maximum if the Bragg condition is fulfilled

$$m\lambda = 2d_{hkl}sin\theta\ , \tag{3.2}$$

where m=1,2,3,… is an integer number and d_{hkl} is the atomic plane spacing.

The lattice mismatch can be found using the following expression:

$$\Delta a_{\perp} = \frac{\lambda_{\alpha}\sqrt{h^2 + k^2 + l^2}}{2}\left(\frac{1}{sin\theta_s} - \frac{1}{sin\theta_f}\right), \tag{3.3}$$

where h, k, l are the Miller indices, and θ_s and θ_f are the maximum intensity angles of the substrate and the film respectively. Larger Miller indices allow to achieve better resolution, therefore for (210) oriented samples we used (8,4,0) diffraction peak with θ_s =

66.9°, whereas for (100) oriented samples (8,0,0) diffraction peak was used with θ_s = 59.7°.

Since our diffractometer does not allow measurement of the absolute values for the angles, it was shown by [Nist06] that the linear approximation

$$sin\theta_f = sin(\theta_s + \Delta\theta) = sin\theta_s + \Delta\theta cos\theta_s \tag{3.4}$$

can be used to derive the following expression for lattice mismatch:

$$\Delta a_\perp = a_s \frac{1-\nu}{1+\nu} \frac{\Delta\theta}{tan\theta_s}, \tag{3.5}$$

where ν = 0.296 is the Poisson ratio and term $\frac{1-\nu}{1+\nu}$ is introduced to correct for the elastic strain.

Measurement of film thickness

On of the most important parameters of thin films is the thickness. Together with additional information such as growth time or Faraday rotation it allows to find the growth rate or the amount of rotation per unit length respectively. In this research work the thickness is measured using an ellipsometer with an infrared grating. The wavelength of the light incident at the sample at θ_i = 45° is changed from 1100 to 1500 nm. The measurement is based on the principle of interference between multiple reflections from film-air and film-substrate interfaces. By measuring the intensity of reflected light at different wavelengths we can observe peaks when constructive interference occurs, Fig. 3.2.

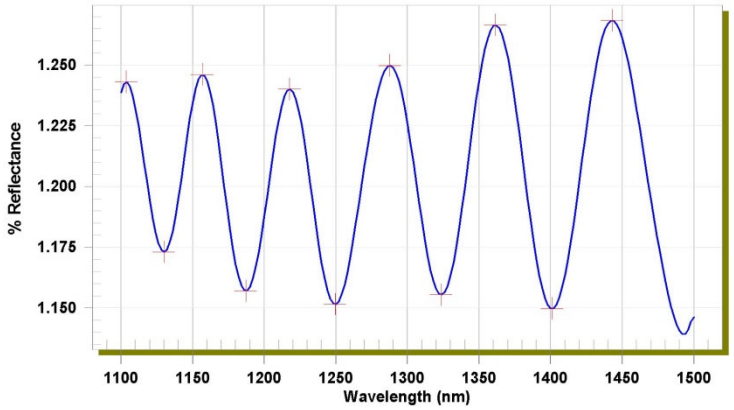

Fig. 3.2. Typical optical signal measured using elipsometer.

Given the wavelengths for the positions of the maxima in the reflected signal the thickness can be determined using the following equation [Nist06]:

$$t = \frac{\frac{1}{2}(N_1 - N_2)\sqrt{n_f^2 - sin^2\theta_i}}{n_f^2\left(\frac{1}{\lambda_1} - \frac{1}{\lambda_2}\right)}, \tag{3.6}$$

where n_f is the index of refraction of the film, λ_1 and λ_2 are the wavelengths of the N_1^{st} and N_2^{nd} peaks respectively.

Measurement of saturation magnetization

The saturation magnetization can be determined using a vibrating sample magnetometer (VSM). It is a widely used instrument for measurements of magnetic properties of a large variety of materials: diamagnetics, paramagnetics, ferromagnetic. This experimental technique was invented [Fon56] and further improved [Fon59] by Simon Foner, a scientist of the MIT, in the sixties. The VSM has a flexible design that

combines high sensitivity and simplicity of operation. Measurements of fields on the order of $5*10^{-5}$ emu are possible in a wide range of magnetic fields. Before the measurements are taken the calibration of the VSM setup has to be performed using a sample with a known magnetic moment (for example pure Ni standard).

A principle of operation of VSM is based on Faraday's Law of Induction, which tells us that a changing magnetic field will induce an electric field. A sample of magnetic material is attached to a non-magnetic holder and placed in between poles of an electromagnet, see Fig. 3.3.

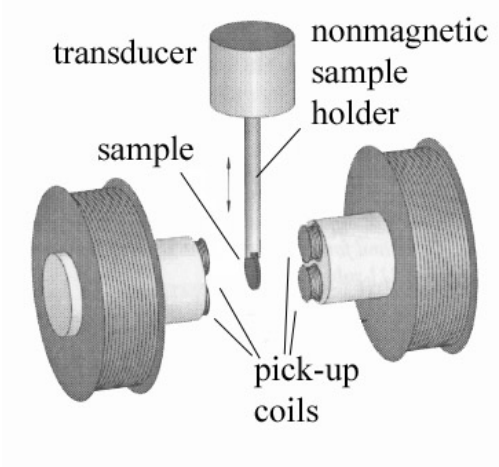

Fig. 3.3. Vibrating Sample Magnetometer Setup.

The magnetic field induces a magnetic moment in the sample. The sample holder is fixed in a transducer which allows vibration along the axis perpendicular to external magnetic field. The transducer vibrates the sample up and down with a set frequency. The changing magnetic flux induces current in a pick-up coil system. This induced signal is detected by

a lock-in amplifier that receives a reference signal of the same frequency as the transducer and can be related to the magnetization of the sample. At small fields there is large increase in the signal because the magnetization in the sample aligns parallel to the external field, but as soon as the sample saturates the slope is significantly reduced. Further increase in the signal with the applied field is due to contribution from the paramagnetic substrate. This contribution from the substrate is significant because of its large volume compared to the thin film, therefore it is necessary to perform the measurements on the substrate material alone and subtract the result from the measurements on the sample.

Ferromagnetic Resonance (FMR) Measurement

Ferromagnetic resonance is a spectroscopic technique to probe the magnetization of ferromagnetic materials. The ferromagnetic effect was found originally by Griffiths [Grif46], and confirmed by Yager and Bozorth [YaBo47]. A theory of the resonance effect was proposed by Charles Kittel in 1947 [Kitt47]. FMR is very similar to nuclear magnetic resonance (NMR) except FMR probes the magnetic moment of electrons and NMR probes the magnetic moment of the atomic nuclei.

The physical principle behind the FMR measurement is the precession of the total magnetic moment of the specimen about the direction of the static magnetic field, and the strong energy absorption from the RF transverse field when its frequency is equal to the precessional frequency. The dynamic motion of the magnetization is described by the Landau-Lifschitz equation:

$$\frac{d\vec{M}}{dt} = -\gamma\vec{M} \times \vec{H}_{eff} - \frac{\alpha\gamma}{M_S}\left[\vec{M} \times \left(\vec{M} \times \vec{H}_{eff}\right)\right], \tag{3.7}$$

where H_{eff} is the resultant magnetic field that combines the applied external field and the internal fields from the presence of material anisotropies and demagnetizing factors, M_S is the saturation magnetization, α is the damping parameter, and γ is the gyromagnetic ratio.

For small excitation powers, the resonance frequency of the magnetization precession is given by [BaWa88]:

$$\left(\frac{\omega}{\gamma}\right)^2 = \frac{1}{M^2}\left[\frac{\partial^2 E}{\partial\theta^2}\left(\frac{1}{sin^2\theta}\frac{\partial^2 E}{\partial\varphi^2} + \frac{cos\theta}{sin\theta}\frac{\partial E}{\partial\theta}\right) - \left(\frac{1}{sin\theta}\frac{\partial^2 E}{\partial\varphi\partial\theta} - \frac{cos\theta}{sin^2\theta}\frac{\partial E}{\partial\varphi}\right)^2\right]. \tag{3.8}$$

In the last equation E is free energy density, described in Chapter 1, and derivatives are taken with respect to the polar angle θ and the azimuthal angle φ of the equilibrium magnetization M_{eq}.

In the most general case of a thin epitaxial garnet film, the anisotropy energy density has three distinct components: stress-induced, growth-induced, and crystallographic or cubic anisotropies [MiDu00]. For (210)-oriented substrates, it can be shown (using the two-parametric model of the growth-induced anisotropy [Esch81]) that the corresponding energy term for orthorhombic anisotropy can be expressed as [BuDu03]:

$$E_G = K_U m_z^2 + K_i m_y^2 + K_{yz} m_y m_z, \tag{3.9}$$

where K_U is out-of-plane uniaxial anisotropy, K_i is the in-plane uniaxial anisotropy, and K_{yz} is the canted orthorhombic anisotropy constants. For the (210)-oriented substrates (see Figure 3.4), the total free energy density of a homogeneously magnetized thin film can be written as

$$E = -\vec{M} \cdot \vec{H} - K_{Ueff} cos^2\theta + K_i \left(sin^2\theta \, sin^2\varphi + \frac{2}{\kappa} sin\theta \, cos\theta \, sin\varphi \right) + E_{cubic}, \tag{3.10}$$

where M is the magnetization, $\kappa = 2K_i/K_{yz}$, $K_{Ueff} = K_U - 2\pi M_S^2$, and H is the applied field. The angles θ and φ are defined in the Fig. 3.4. The cubic energy density for a (210)-oriented garnet thin film is given by

$$E_{cubic} = K_1 \left\{ \frac{4}{25} cos^4\theta - \frac{24}{50} cos^3\theta \, sin\theta \, sin\varphi + \left[\frac{26}{50} + \frac{24}{50} cos2\varphi \right] cos^2\theta \, sin^2\theta \right. \tag{3.11}$$
$$\left. + \frac{24}{50} cos\theta \, sin^3\theta \, sin^3\varphi + \left[\frac{29}{50} + \frac{21}{50} cos2\varphi \right] sin^4\theta \, sin^2\varphi \right\}$$

where K_1 is the cubic anisotropy constant.

A schematic of an in-house FMR system, built by our research group [Zhan04], is shown in the Fig. 3.5. During the experiment the sample is placed film side down on a microstrip line. The signal from the microwave source passes through the stripline and gets partially absorbed by the sample. The amount of absorption depends on the frequency of the RF signal and the applied external magnetic field. When the resonance condition is matched the absorption in the sample is largest. The rest of the energy is reflected back towards the detector diode which converts it into the measurable DC

voltage. The frequency of the microwave source is kept fixed whereas the magnetic field is being changed within the range of interest. The reflected signal is

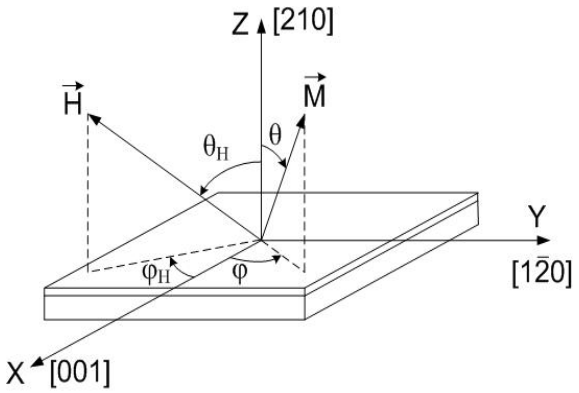

Fig. 3.4. Film coordinate system for (210)-oriented thin garnet film.

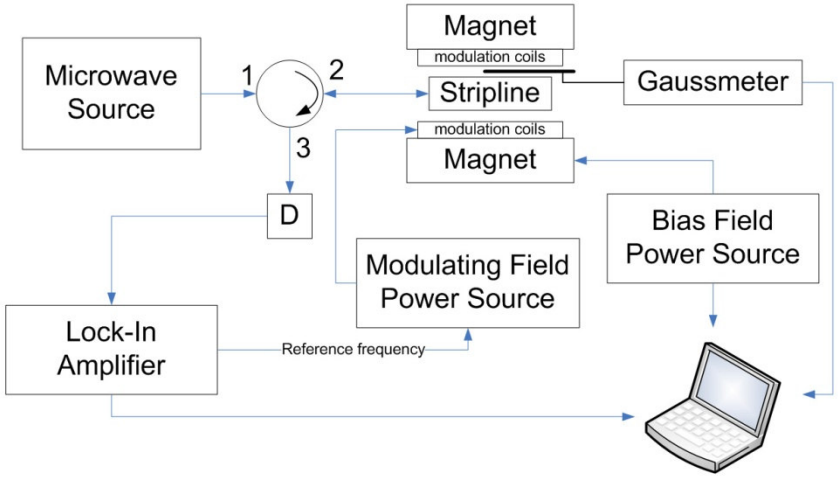

Fig. 3.5. Schematic representation of the FMR system.

measured using lock-in amplifier with the reference signal of the same frequency as a small modulation field superposed on the DC magnetic field. The output of the lock-in

amplifier is proportional to the derivative of the absorption peak (see Fig. 3.6). Using these data the resonance field can be determined for different orientations of the sample with respect to the external field (see Fig. 3.7). The anisotropy fields can be obtained by numerically fitting the experimental data using the equation (3.8) for the resonance frequency.

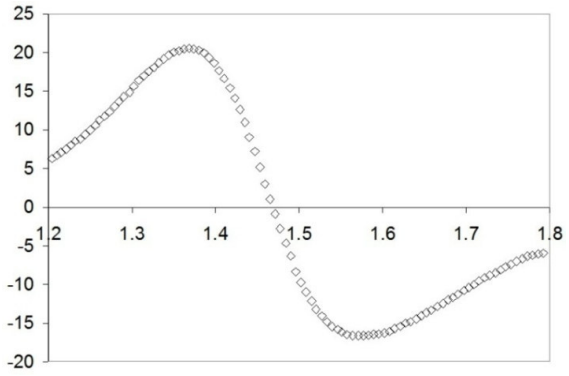

Fig. 3.6. Typical signal measured in the FMR experiment. The x axis is the magnitude of the magnetic field in kOe.

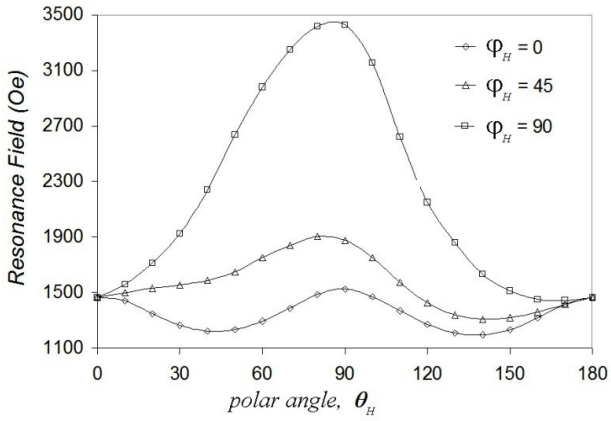

Fig. 3.7. Dependence of the ferromagnetic resonance field on the orientation of the sample.

Design of magneto-optic imaging system

Usage of the magnetic garnet films for imaging of stray magnetic fields requires a special imaging apparatus. The system requirements include the ability to obtain low magnification images of tape with as large a field of view as possible while having submicron resolution capability that is limited only by optical diffraction and not by an inherent characteristic of the garnet. An optimal imaging garnet needs to have good sensitivity and continuous response from fields produced by the magnetic sample, estimated to be in the range of 1 to 30 Oe [KraST11]. The garnet should provide an accurate replication of the field pattern in the media with minimal artifacts related to the garnet. Garnet artifacts include domain walls, either larger planar zig-zag walls or serpentine perpendicular walls or domains, defects in the garnet such as scratches, growth defects, and other domain wall pinning defects. High Faraday rotation is also desirable.

Three important issues need to be taken into account while designing a stage and garnet holder: field of view, area of tape under the garnet, and area of interest for examination. The field of view is dependent on the microscope objective and video optics and ranges from tens of microns to a few millimeters. The area of tape observable under a piece of garnet is approximately one centimeter square. It is possible to use larger pieces of garnet, but obtaining a good, uniform contact between the tape and the garnet becomes an issue. The area of interest for examination can be tens of millimeters or larger. Registration of events is as important as being able to show their spatial relationship.

The schematic of the in-situ magneto-optic system is shown in Fig. 3.8. Schematic of the magneto-optic imaging system.Fig. 3.8.

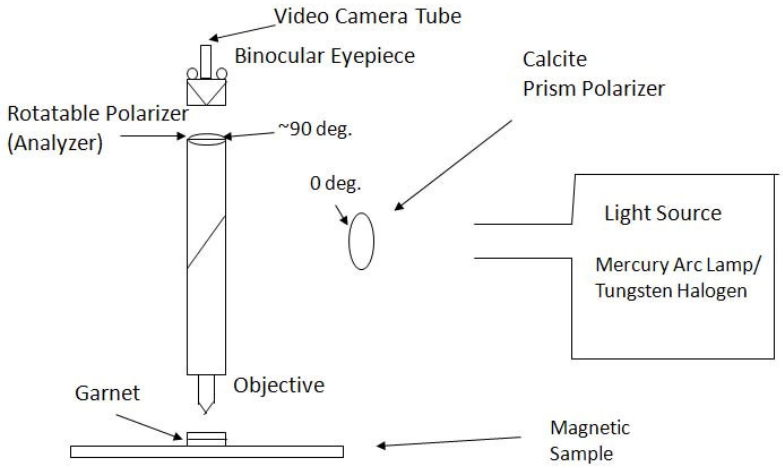

Fig. 3.8. Schematic of the magneto-optic imaging system.

The apparatus consists of a polarized light microscope with a specially designed garnet holder and stage. The microscope objectives range in power from 2.5X to 50X. Two light sources are available for illumination, a mercury arc lamp and a tungsten halogen lamp. The magnetic patterns on the imaged sample can be observed through the binocular eyepiece or captured by a digital video camera as high resolution still images. A pair of linear encoders is attached to the microscope stage to measure its position. A software interface was developed using Labview to control the camera exposure and to incorporate the linear encoder position onto the digital image. An overlay on the video image provided real-time display of the horizontal and vertical coordinates of the stage

which was useful for indexing events that occurred over a distance larger than the microscope field of view.

A photograph of the garnet imager stage is shown in Fig. 3.9a. The garnet is mounted on an aluminum plate that is inserted into a dove-tailed slider. The entire assembly can be slid along a milled slot on the base plate of the stage. The range of travel matches that of the microscope stage, allowing one to observe up to 6 inches of tape without moving the tape. Two viewing slots on either side of the garnet allow for alignment of the tape, as the garnets used here had a reflective coating on the backside. A spring-loaded tape clamp is situated at each end of the stage. In normal operation, a length of tape is drawn out of its cartridge and placed on the stage. Once this reference point is set, all measurements are relative to this setting.

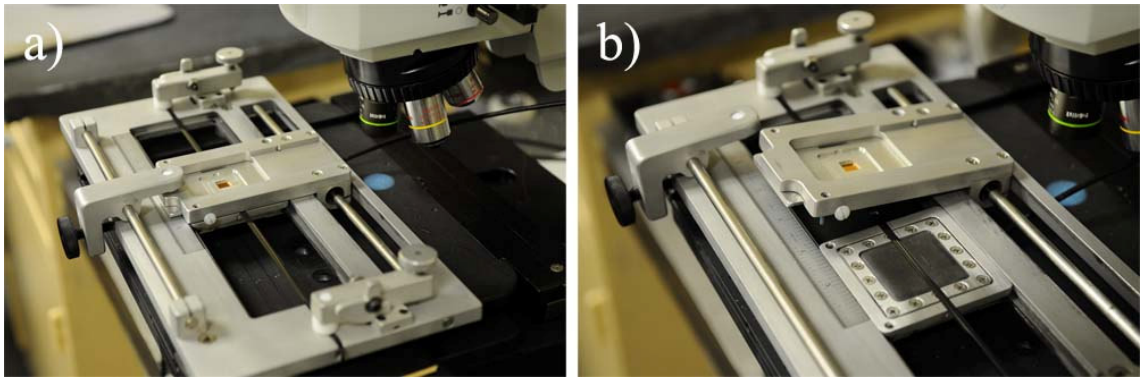

Fig. 3.9. a) garnet imager stage on polarized light microscope b) air bladder which is used to provide good contact between tape and garnet.

The key to getting uniform contact between the tape and the garnet over the entire surface of the garnet is to place an air bladder under the sample stage [KraDo07]. The

bladder is shown in Fig. 3.9b. The tape can be easily slid across the stage when the bladder is deflated. For imaging, the top plate is clamped down and the bladder is inflated with a small hand-pump, providing uniform contact between the tape and the garnet over the entire garnet area. **Error! Reference source not found.**Although the garnet has a protective coating over the mirror, the tape surface is abrasive. Repeated dragging of the tape over the garnet, as would happen with a spring-based mechanism, leads to failure of the protective coating and degradation of the mirror. The arrangement developed here leads to consistent pressure between the tape and the garnet and vastly improves the quality and uniformity of our images.

One question that can be asked is how sensitive are the garnet indicator films. To help answer this, a series of audio tapes were recorded with a reference track at 3 kHz at 0 dB and a 314 Hz signal at levels ranging in -10 dB steps from 0 to -50 dB. Images of the low frequency track (Fig. 3.10) reveal a gradual weakening of the visible track to -30 dB. The signal at -40 dB is discernable but garnet sample artifacts dominate the image. At -50 dB, a very faint signal is visible with this garnet, but this would not be discerned without prior knowledge of the existence of the signal. Video signal enhancement could improve the low frequency signal, however this signal is overwhelmed by structural artifacts in the garnet and contamination in the microscope optics.

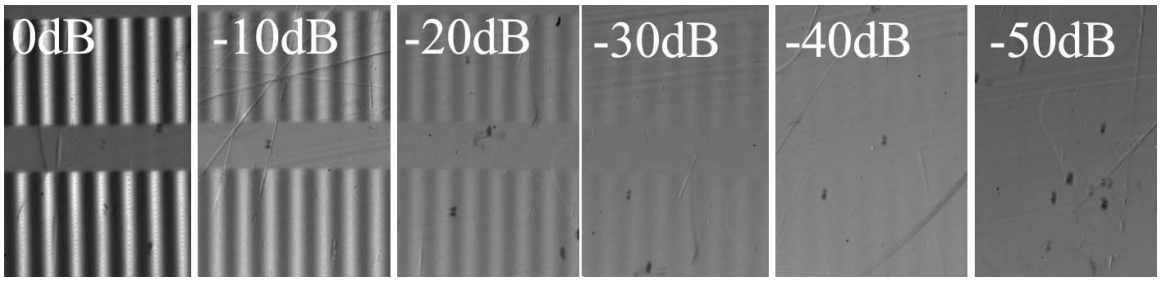

Fig. 3.10. Images from stereo audio tape, 314 Hz signal at signal strengths indicated.

Chapter Bibliography

[BaWa88] L. Baselgia, M. Warden, et al., "Derivation of the resonance frequency from the free energy of ferromagnets", *Physical Review B*, **38**, 2237 (1988).

[BuDu03] V.I. Butrim, S.V. Dubinko, and Yu.N. Mitsai, "Anisotropy and phase states of garnet ferrite films with misoriented surfaces", *Physics of the Solid State*, **45**, 1102 (2003).

[Esch81] A.H. Eschenfelder, "Magnetic Bubble Technology", *Springer-Verlag*, New York (1981).

[Fon56] S. Foner, "Vibrating Sample Magnetometer", *Review of Scientific Instruments*, **27**, 548 (1956).

[Fon59] S. Foner, "Versatile and Sensitive Vibrating Sample Magnetometer", *Review of Scientific Instruments*, **30**, 548-557 (1959).

[Grif46] J.H.E. Griffiths,"Anomalous High-frequency Resistance of Ferromagnetic Metals", *Nature*, **158**, 670 (1946).

[Hol04] C. Holthaus, "Development of sensitive indicators for magneto-optical pattern recognition", *PhD Dissertation Thesis*, University of Osnabrück (2004).

[Kitt47] C. Kittel, "Interpretation of Anomalous Larmor Frequencies in Ferromagnetic Resonance Experiment", *Physical Review*, **71**, 270 (1947).

[KraDo07] C. S. Krafft, J. B. Dottellis, US Patent No. 7 239 332 B1, (2007).

[KraST11] C. Krafft, S. Tkachuk, G. Lang, D. Bowen, I.D. Mayergoyz, "Magneto-Optic Indicator Films for Forensics (invited)", on-line publication in *MRS Online Proceedings (part of Cambridge Journals Online),* January 2011.

[MiDu00] R.M. Mikherskii, S.V. Dubinko, “Epitaxial Garnet Ferrite Films with Anisotropy of the Inclined Easy Plane Type”, Tech Phys Lett., 26, 265 (2000).

[Nist06] I. Nistor, “Development of magnetic field sensors using Bismuth-substituted garnets thin films with in-plane magnetization”, *PhD Dissertation Thesis*, University of Maryland (2006).

[YaBo47] W.A. Yager, R.M. Bozorth, “Ferromagnetic Resonance at Microwave Frequences”, *Physical Review*, **72**, 80 (1947).

[Zhan04] J. Zhang, “Growth and FMR characterization of in-plane magnetization garnet thin films”, *Master Thesis*, University of Maryland (2004).

Chapter 4 : Plasmon Resonance Enhancement of Magneto-Optic Effects

It is known that on the microscopic level magneto-optic (Faraday and Kerr) effects are controlled by spin-orbit coupling. Spin-orbit (SO) interaction enters into the Hamiltonian from a nonrelativistic approximation to the Dirac equation [Sak67]. This approach gives rise to the Pauli SO term

$$\hat{H}_{SO} = \frac{\hbar}{4m^2c^2}(\nabla V \times \hat{p}) \cdot \hat{\sigma}, \tag{4.1}$$

where $\hbar$ is Planck's constant, m is the mass of a free electron, c is the velocity of light, $\hat{p}$ is the momentum operator, V is the potential, and $\hat{\sigma} = (\sigma_x, \sigma_y, \sigma_z)$ is the vector of Pauli spin matrices. This equation suggests that the Faraday effect may be enhanced by enhancing electric field in the area of interest. One way to excite strong local electric fields is through plasmon resonances in metallic (silver or gold) nanoparticles embedded in magneto-optic media. Experimental confirmation of such enhancement of magneto-optic effects was recently reported in [Fuji08, Tom06, UcMa09]. The efficient plasmon resonance enhancement of magneto-optic effects requires thorough understanding of how the shape and the spacing of nanoparticles affect plasmon resonance wavelength and mode coupling.

Plasmon resonances are electrostatic in nature and happen at frequencies for which permittivity of metallic nanoparticles is negative and their dimensions are small in comparison with wavelength [May10]. Plasmon resonances appear at specific negative

values of dielectric permittivity ε_k for which source-free electrostatic fields may exist. In order to find these negative values of ε_k for which plasmon resonances occur, the eigenvalues of the following integral equation need to be found:

$$\sigma_k(Q) = \frac{\lambda_k}{2\pi} \oint_S \sigma_k(M) \frac{\partial G(M,Q)}{\partial n_Q} ds_M \,, \tag{4.2}$$

where $\sigma_k(M)$ has a meaning of surface electric charges on the particle boundary S that produce electric field of the k^{th} plasmon mode, and $G\ (M, Q)$ is Green's function which accounts for the garnet plane boundary. The eigenvalues λ_k of the integral equation given above can be related to the negative resonance values of dielectric permittivity ε_k by the formula

$$\lambda_k = \frac{\varepsilon_k - \varepsilon_0}{\varepsilon_k + \varepsilon_0}, \tag{4.3}$$

Green's function can be expressed as follows:

$$G\ (M,Q) = \frac{1}{r_{MQ}} \pm \frac{\varepsilon_g - \varepsilon_0}{\varepsilon_g + \varepsilon_0} \frac{1}{r_{M'Q}} \tag{4.4}$$

with the sign of the second term depending on whether nanoparticles are placed on the garnet surface (-) or embedded in garnet (+), see Fig. 4.1. Point M' is the mirror-image of point M with respect to the garnet plane boundary and ε_g is the garnet permittivity.

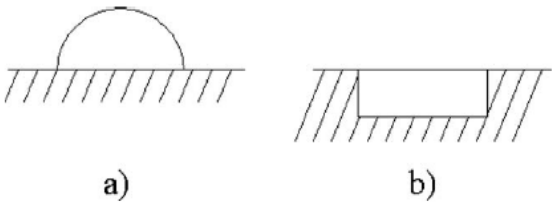

Fig. 4.1. Schematic image of nanoparticles (a) placed on the garnet surface; (b) embedded in garnet.

The resonance frequencies ω_k can be found from the dispersion relation

$$\varepsilon_k = \varepsilon'(\omega_k) \,, \tag{4.5}$$

where ε' is the real part of dielectric permittivity $\varepsilon(\omega)$ of metallic nanoparticles. It is clear from the equations (4.2)-(4.4) that plasmon resonance wavelengths are invariant with respect to scaling of dimensions of nanoparticles, i.e., they depend on the shape of nanoparticles but not their dimensions provided that resonance wavelength is much larger than dimensions of nanoparticles. This means that if gold or silver nanoparticles embedded into garnets have the same shape but different dimensions, then they will still simultaneously resonate at the same wavelength of incident optical radiation and collectively contribute to the enhancement of magneto-optic effects.

In order to explain the coupling of incident optical radiation to specific plasmon modes, boundary charges $\sigma(M, t)$ induced on particle boundaries during the excitation process can be expanded in terms of plasmon modes $\sigma_k(M)$,

$$\sigma(M,t) = \sum_{k=1}^{\infty} a_k(t)\sigma_k(M)\,. \tag{4.6}$$

It has been shown [May07] that when the incident optical radiation has the same frequency as the resonance frequency ω_k of the k^{th} plasmon mode, the coefficient a_k(t) in expansion (4.6) is strongly dominant and under steady state conditions $a_k^{ss}(t)$ is given by the following formula:

$$a_k^{ss}(t) = -(\boldsymbol{E}_0 \cdot \boldsymbol{p}_k)\frac{\varepsilon'(\omega_k) - \varepsilon_0}{\varepsilon''(\omega_k)}\cos\omega_k t \tag{4.7}$$

where $\boldsymbol{E}_0$ is the electric field of the incident radiation, p_k is the dipole moment of the k^{th} plasmon mode, while ε"(ω) is the imaginary part of ε(ω).

Equation (4.7) suggests that the desired plasmon modes are most efficiently excited when the direction of polarization of incident optical radiation coincides with the direction of the dipole moment $\boldsymbol{p}_k$ of the plasmon mode. Such a conclusion is consistent with "anisotropy of light coupling" observed in [Fuji08]. This formula also reveals that the resonance electric fields depend on the ratio of real to imaginary parts of dielectric permittivity of metallic nanoparticles at the resonance frequency. For gold and silver this ratio is the largest (about 16 for Au and about 85 for Ag) in the freespace wavelength ranges of 700-900 and 800-1100 nm respectively.

It has been shown in [May07] that the width of the plasmon resonances can be evaluated by steady state expansion coefficient for off-resonance excitation with frequency ω_0:

$$a_k^{ss}(t) = (\boldsymbol{E}_0 \cdot \boldsymbol{p}_k) C(\omega_0) \cos(\omega_0 t + \varphi), \tag{4.8}$$

where

$$C(\omega_0) = \sqrt{\frac{[\varepsilon'(\omega_0) - \varepsilon_0]^2 + [\varepsilon''(\omega_0)]^2}{[\varepsilon_k - \varepsilon'(\omega_0)]^2 + [\varepsilon''(\omega_0)]^2}} \tag{4.9}$$

The last formula reveals optical frequency range for which plasmon resonances may enhance magneto-optic effects.

The numerical simulations and the quasistatic analyses of the plasmon resonances in hemispherical type gold nanoparticles based on equations (4.2) – (4.5) are reported in [May10]. This kind of nanoparticles can be experimentally obtained by depositing a thin layer (about 4 nm thick) of gold on a garnet substrate and subsequently annealing it at temperature around 800 °C [Fuji08, UcMa09]. Fig. 4.2 shows the dependence of resonance wavelength on the height to radius ratio for a single hemispherical particle.

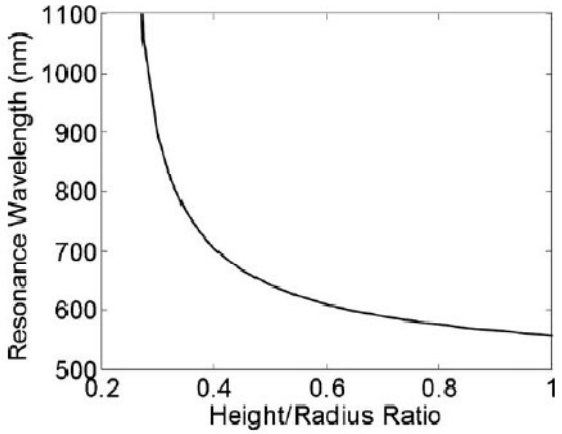

Fig. 4.2. The dependence of the resonance wavelength on the height of single hemispherical particle.

The experimental data [Fuji08] demonstrate that the largest magneto-optic effect enhancement was achieved at 620 nm wavelength, which means height to radius ratio of about 0.5 according to the simulation results. The last figure also indicates that by reducing the height to radius ratio of the gold nanoparticles to about 0.3 it is possible to shift resonance wavelength into 800-1100 nm range where the $\varepsilon'(\omega_k)/\varepsilon''(\omega_k)$ ratio for gold is the largest and therefore plasmon resonances are most pronounced. The results of the simulations performed for two and four adjacent hemispherical particles are presented in the next figure

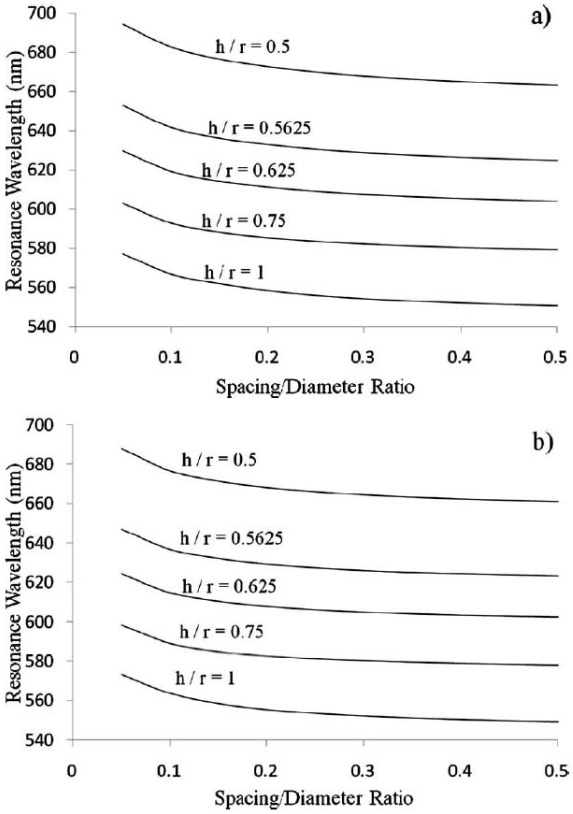

Fig. 4.3. The dependence of the resonance wavelength on the spacing between (a) two and (b) four gold hemispherical nanoparticles for different values on height to radius ratio.

These calculations show that particles do not “feel” each other as long as their spacing-to-diameter ratio is larger than 0.3, and the resonance wavelength for a group of particles is practically the same as for single particle. Reduction in spacing-to-diameter ratio below 0.3 results in some increase of the resonance wavelength. It is important to mention that due to the small size of the nanoparticles in comparison with free-space wavelength of the incident radiation only dipole-type resonance modes can be efficiently coupled. The dipole moments of these modes are parallel to the garnet boundary plane which is required for the efficient excitation of plasmon resonances.

In order to have significant magneto-optic effect enhancement it is necessary that the electric fields of the plasmon resonance modes penetrate deep into magneto-optic media. The nanoparticles of cylindrical shape are beneficial for such purposes. Fig. 4.4 and Fig. 4.5 represent the results of the computations for the particles of cylindrical shape embedded in garnet films.

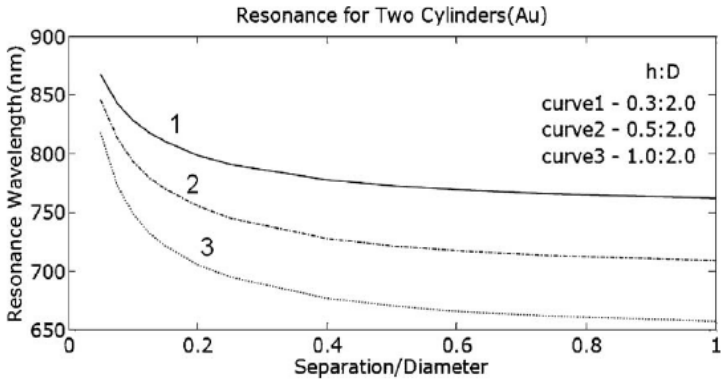

Fig. 4.4. Resonance wavelength as a function of particle geometry.

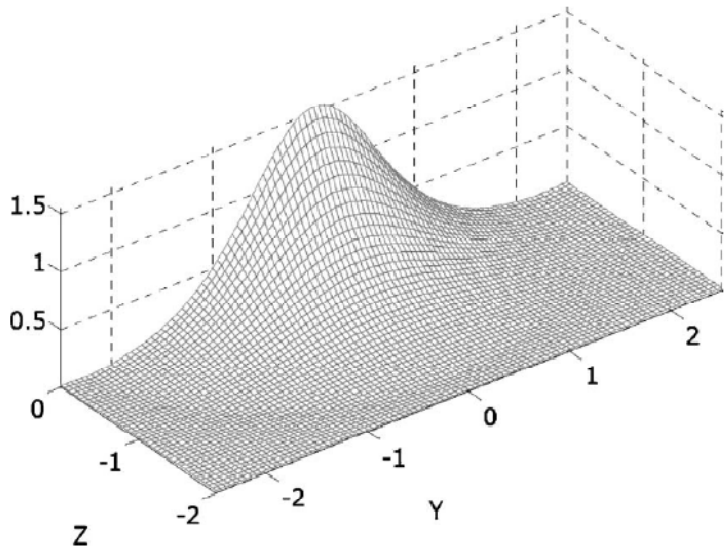

Fig. 4.5. Distribution of plasmon electric field in the midplane between particles.

It is clear from Fig. 4.4 that the resonance wavelength can be shifted in the region of 800 – 1100 nm by controlling the aspect ratio and the separation-to-diameter ratio of these particles.

Chapter Bibliography

[Fuji08] R. Fujikawa, A. V. Baryshev, J. Kim, H. Uchida, and M. Inoue, J. Appl. Phys. 103, 07D301 (2008).

[May07] I. D. Mayergoyz, Z. Zhang, and G. Miano, Phys. Rev. Lett. 98, 147401 (2007).

[May10] I.D. Mayergoyz, G. Lang, L. Hung, S. Tkachuk, C. Krafft, and O. Rabin, J. Appl. Phys., 107, 09A925 (2010).

[Sak67] J. J. Sakurai, *Advanced Quantum Mechanics*, (Addison-Wesley, Reading, MA, 1967).

[Tom06] S. Tomita, T. Kato, S. Tsunashima, S. Iwata, M. Fujii, and S. Hayashi, Phys. Rev. Lett. 96, 167402 (2006).

[UcMa09] H. Uchida, Y. Masuda, R. Fujikawa, A. V. Baryshev, and M. Inoue, J. Magn. Magn. Mater. 321, 843 (2009).

Chapter 5 : Magneto-optical imagers based on thin garnet films

It has been recognized that the development of high sensitivity garnet films for nonscanning imaging applications is of great interest. Indeed, garnet based magneto-optical indicators provide unique capabilities for real time detection and visualization of two-dimensional magnetic field patterns. It has been long understood that the sensitivity of garnet films as magneto-optical imagers is determined by their anisotropy properties which are, in turn, controlled by crystallographic orientations of substrates utilized in the garnet growth process. This is because the crystallographic orientations of the substrates profoundly influence the form and nature of growth induced anisotropies. In this respect, garnet films grown on (210)-oriented substrates are of special interest due to their unique growth induced anisotropy properties that may result in an easy plane of magnetization inclined with respect to the film plane. This inclined easy plane of magnetization may lead to low saturation fields and high magnetic field sensitivities.

Study of thin garnet films grown on (210)-oriented substrates

In the absence of the external magnetic field and neglecting usually small cubic anisotropy, (3.10) can be written as

$$E = -K_{Ueff}cos^2\theta + K_i\left(sin^2\theta\ sin^2\varphi + \frac{2}{\kappa}sin\theta\ cos\theta\ sin\varphi\right) \tag{5.1}$$

It is apparent, that if the following condition is satisfied:

$$K_i = -\kappa^2 K_{Ueff} \tag{5.2}$$

then (5.1) can be written in the form

$$E = -K_{Ueff}(cos\theta + \kappa\, sin\theta\, sin\varphi)^2. \tag{5.3}$$

For $K_{Ueff} < 0$, it can be seen that the energy is at a minimum if the magnetization is in the plane determined by the equation

$$tan\theta\, sin\varphi = -1/\kappa. \tag{5.4}$$

This plane is inclined with respect to the film normal by the angle $\theta = arctan|1/\kappa|$, see Fig. 5.1. Thus, with increasing $|\kappa|$ the angle increases and the plane turns perpendicular to the film plane. The magnetization is able to move freely in this plane, which provides the high sensitivity of (210)-oriented epitaxial thin garnet films.

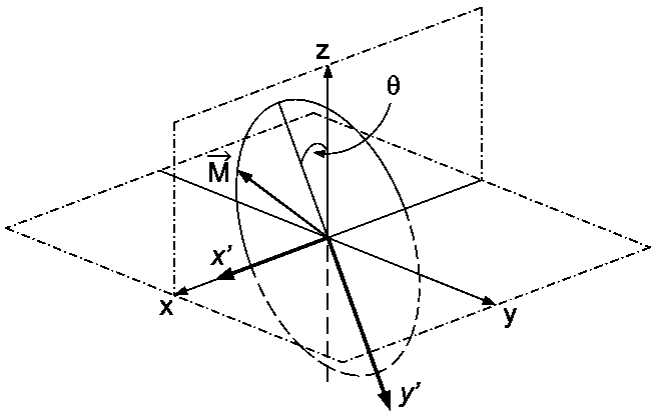

Fig. 5.1. The easy plane of magnetization. Coordinate axes x, y, and z are chosen to coincide with crystallographic directions [001], [1$\bar{2}$0], and [210], respectively. Axes *x'* and *y'* are in the easy magnetization plane.

In order to verify the above theory experimentally the epitaxial films were grown by the liquid phase epitaxy technique from a PbO-Bi_2O_3-B_2O_3 flux on (210)-oriented (Ca, Mg, Zr)-$Gd_3Ga_5O_{12}$ substrates with expanded lattice constant (a=12.498Å). Several melts were designed based on the following requirements: crystallographic lattice matching between the film and the substrate, high Bi incorporation to enhance the Faraday rotation, and optimal quantity of rare-earth elements to obtain anisotropy constants that would satisfy condition (5.2). The goal has been to create a melt which would allow us to grow films with an easy magnetization plane.

In designing the melts, it has been taken into account that large Bi ions are also part of a garnet phase and are needed to increase magneto-optical activity, small Lu ions help to match the crystallographic lattice constant, Gd is used to reduce temperature dependence of film properties, whereas Pr reduces out-of-plane uniaxial anisotropy. In order to adjust the saturation magnetization Fe has been partially substituted with Ga ions. The 5:1 ratio of Fe:Ga has been used for all the melts. The cation oxide percentages for the melt iterations that have been used to grow samples are given in Table 5-1.

Table 5-1. Cation Oxide Percentages for the Melt Iterations

Melt	Pr	Lu	Gd
A	0.0373	0.0932	0.5592
B	0.1724	0.0862	0.4310
C	0.1452	0.0907	0.4537
D	0.1335	0.0927	0.4635
E	0.1217	0.0811	0.4868
F	0.1068	0.0971	0.4857

The properties of the samples grown from the above melts along with their anisotropy fields are summarized in Table 5-2

Table 5-2. Anisotropy fields and properties of thin garnet films

Sample	Growth Rate (μm/min)	Θ_F (deg/cm)	Δa (Å)	Hk_{Ueff} (Oe)	Hk_1 (Oe)	Hk_i (Oe)	Hk_{yz} (Oe)	κ	H_S (Oe)	χ
A1	0.697	-11486	-0.001	958	-120	791	444	3.6	153	-15.3
B1	0.259	-11015	-0.008	-757	-99	981	-365	-5.4	775	22.2
C1	0.307	-11623	-0.007	-422	-97	874	-328	-5.3	336	13.7
D1	0.334	-11236	-0.005	-285	-149	1098	487	4.5	212	5.3
E1	0.554	-13531	-0.014	-98	-220	1490	466	6.4	143	2.7
F1	0.433	-8077	-0.007	72	-135	886	334	5.3	182	-2.3
F2	0.594	-11485	-0.013	22	-254	1457	361	8.1	111	-1.0
F3	0.654	-11953	-0.015	-107	-317	2052	542	7.6	61	3.0
F4	0.729	-12734	-0.019	-378	-422	2591	599	8.7	68	10.9

In this table Θ_F is specific Faraday rotation, $\Delta a = a_s - a_f$ – lattice mismatch, $\kappa = 2K_i/K_{yz}$ - geometrical parameter, $\chi = -\frac{4K_{Ueff}K_i}{K_{yz}^2}$ - easy magnetization plane ration, where χ=1 if (5.2) is fulfilled, and H_S – saturation field. Anisotropy fields Hk_{Ueff}, Hk_1, Hk_i, and Hk_{yz} can be related to the anisotropy constants through the saturation magnetization M_S in the following way $H_{kx} = {}^{2K_x}/_{M_S}$.

The initial melt A had low Pr content and allowed us to grow only samples with strong out-of-plane magnetization. Sample A1, grown from this melt, has a large positive Hk_{Ueff} and therefore a negative coefficient χ. The saturation field is relatively small due to the out-of-plane nature of the magnetization in the film. The next melt iteration (B) had too much Pr and produced samples with strong in-plane magnetization. Decreasing Pr content in the next melt iterations (C, D, and E) helped to fix this problem and led to the increase in Hk_{Ueff}. A final iteration of the melt (E) allowed us to grow a sample (E1) with

the easy magnetization plane ratio $\chi = 2.7$ and a small negative uniaxial anisotropy. A small saturation field together with high value of the specific Faraday rotation angle indicates high sensitivity of this film.

It was interesting to investigate the dependence of the anisotropy fields on the growth conditions for the samples grown from the same melt. For this purpose melt F was designed based on the previous study of the anisotropy fields for various melt compositions. Several samples (F1-F4) were grown at different growth temperatures keeping rotation rates constant. It was observed that as the growth rate goes up the specific Faraday rotation also increases, which suggests that incorporation of Bi becomes larger. At the same time out-of-plane uniaxial anisotropy goes down and in-plane orthorhombic anisotropy goes up with the growth rate, which suggests that Pr incorporation increases as well. This is further supported by the increase in the lattice mismatch parameter Δa (See Table 5-2).

The values of the easy plane ratio are plotted vs. growth rates in Fig. 5.2. The dependence of χ on the growth conditions in the negative region is small while in the positive region it is steep. This kind of behavior makes it very difficult to match exactly condition (5.2).

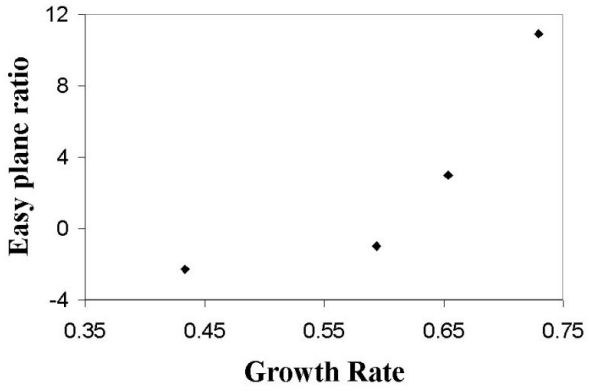

Fig. 5.2. Easy plane ratio as a function of growth rate for the samples based on melt F.

Sample F3 with ratio χ=3 shows very good properties for an MO indicator. It has very low saturation field and high specific Faraday rotation angle. The optical loops of the samples F3 and F1 are compared in Fig. 5.3

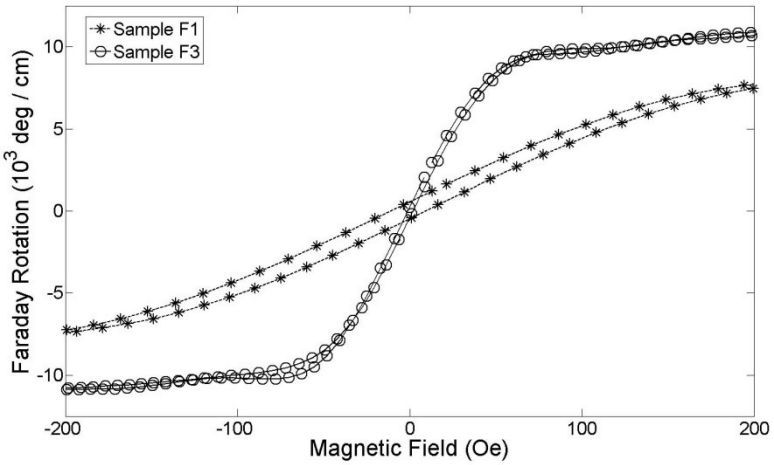

Fig. 5.3. Hysteresis loops for the samples F1 and F3.

It is easy to observe how the slope of the loops becomes steeper as the relation between anisotropy constants approaches condition (5.2). An important figure of merit is the saturation field. The smaller the saturation field the higher the sensitivity of the film, assuming the maximum Faraday rotation is constant. The reduction in H_S along with increase in Faraday rotation angle θ_S is clearly seen from Fig. 5.3. Typically, strong out-of-plane films have very low saturation fields. But as demonstrated in Table 5-2, films with easy magnetization plane may have even smaller values of H_S (compare samples A1 and F3).

Another important observation is that the film with χ-ratio closest to one does not always have the smallest saturation field (see, for example, samples E1 and F3). The reason is that at the easy magnetization plane the induced anisotropy energy is small. Therefore the cubic anisotropy becomes of comparable value and cannot be neglected. The behavior of the anisotropy energy density in the easy plane due to both terms was numerically investigated and corresponding results plotted in Fig. 5.4. The line of circles indicates zero value of the energy in the easy plane. Diamonds show the case when the cubic anisotropy energy is neglected and the induced energy term is calculated using experimentally obtained coefficients for sample F3. The cubic term by itself is plotted with squares, whereas the total anisotropy energy is labeled by triangles. It is clearly seen from the figure that the cubic anisotropy energy almost completely compensates the deviations due to the induced anisotropy energy.

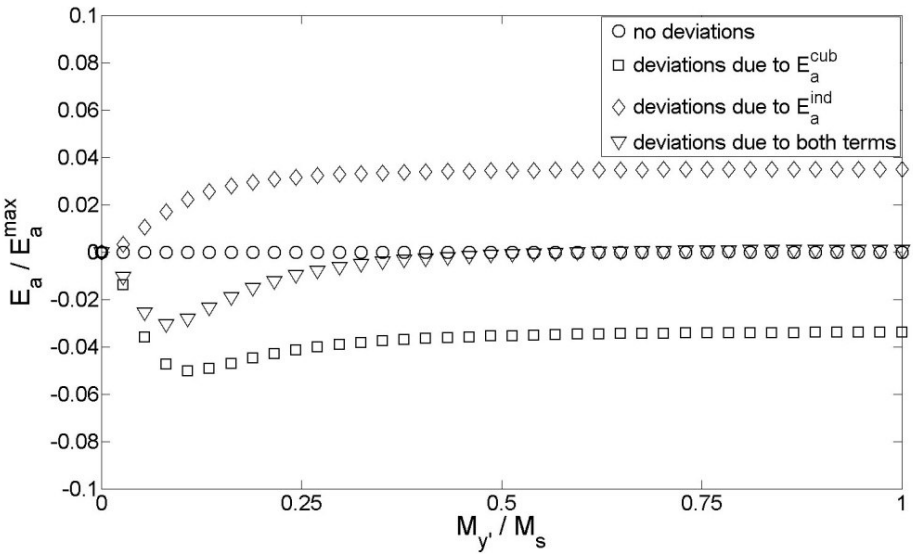

Fig. 5.4. Normalized anisotropy energy density as a function of normalized projection of magnetization on the y' axis.

The imaging capabilities of thin garnet films of composition $(Bi,Gd,Lu,Pr)_3(Fe,Ga)_5O_{12}$ grown on (210)-oriented substrates have been studied by imaging of data tracks recorded on digital data storage (DDS) tapes. It has been demonstrated that the film thickness reduction by chemical etching alleviates the obscuring effects of film domain structures on intrinsic magneto-optical images. In this way, the film etching enhances the clarity and spatial resolution of magneto-optical images. Typical domain structure of such films is shown in Fig. 5.5. These intrinsic domain structures are weakly influenced by the imaged patterns and strongly obscure them. To minimize these obscuring effects, a (210)-oriented garnet film with the original thickness of 3.85 μm has been sequentially etched in hot phosphoric acid for different periods of time. It has been observed that the reduction in film thickness through etching

has resulted in appreciable reduction in domain size (see Table 5-3). For instance, the reduction in thickness to 1.73 μm has resulted in about 40% reduction in domain size (see Fig. 5.5b).

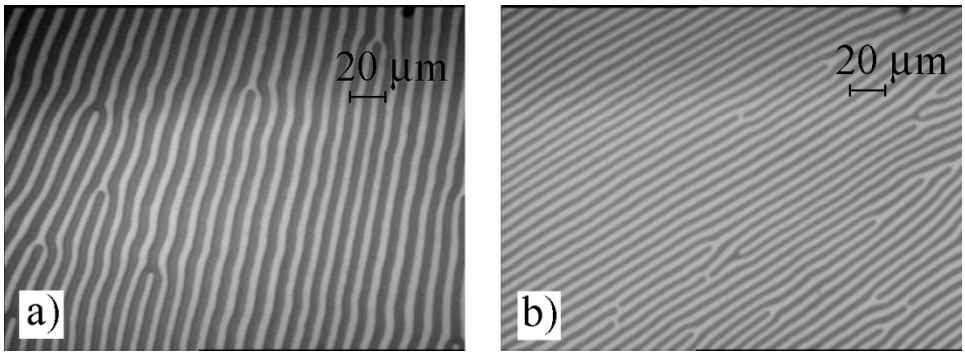

Fig. 5.5. Example of the domain structures in garnet films: a) before etching, - the thickness of the film is around 3.85 µm., the width of the stripe domain is approximately 5.5 µm., b) after etching, - the thickness of the film is around 1.73 µm., the width of the stripe domain is approximately 3.3 µm.

Table 5-3. Domain size vs film thickness

Etch Step	Thickness (µm)	Domain Size (µm)
1	3.85	5.46
2	2.96	5.25
3	2.68	4.98
4	1.97	4.95
5	1.73	3.27
6	0.42	Single domain state

Examples of the images of the periodic magnetization patterns recorded on DDS tape are shown in Fig. 5.6. Fig. 5.6(a) presents the image obtained prior to the etching when the domain structure of garnet film is shown in Fig. 5.5(a). It is apparent that only low

frequency recorded magnetization patterns are barely observable in this image; the high frequency patterns are completely obscured by the film domain structure. On the other hand, Fig. 5.6(b) – (d) are the images of the recorded magnetization pattern obtained by using the same garnet films with (etched) reduced thickness of about 0.4 μm. It is apparent that these images clearly reveal the recorded magnetization patterns with clarity and intricate details. It can be inferred from these images that there are several tracks of periodically recorded patterns of different densities. It is also clear that (210)-oriented garnet films can provide submicron resolution at least on the level of 500nm. Thus, it can be concluded that (210)-oriented garnet films may indeed provide unique capabilities for submicron magneto-optical imaging.

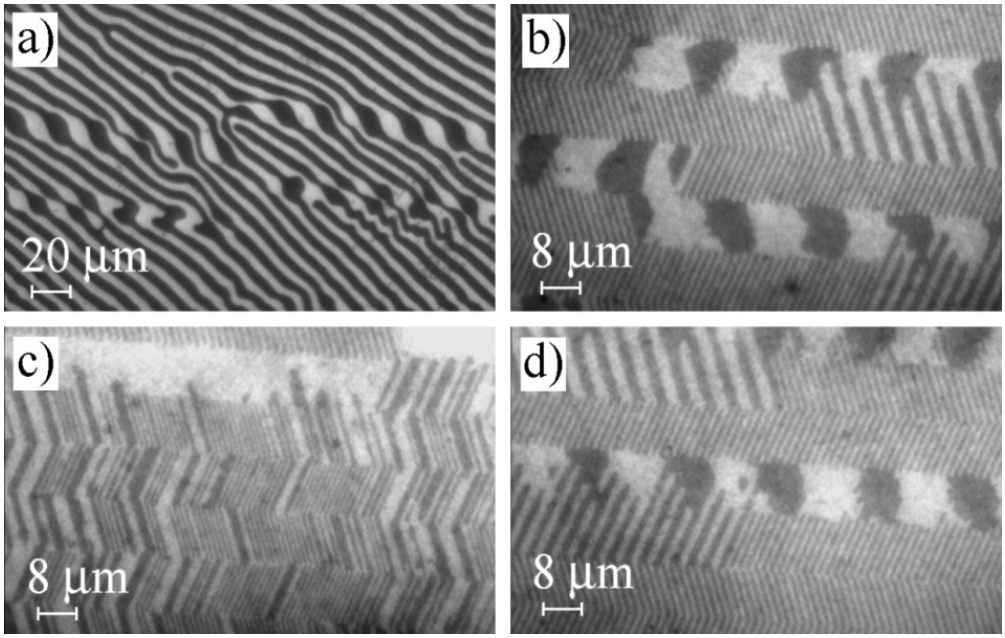

Fig. 5.6. Image of a DDS tape: (a) using unetched garnet film of thickness around 3.85 μm, and (b), (c), (d) using etched garnet film of thickness around 0.4 μm.

Etching of garnet films grown on (100) and (210)-oriented substrates

The observation of significant improvement in the imaging capabilities of (210) oriented garnet films with thickness reduction lead us to the next set of experiments performed to study the effects of etching on (100) oriented films. The samples of the following generic composition (Bi, Pr, Lu, Gd)$_3$(Fe, Ga)$_5$O$_{12}$ were grown by the liquid phase epitaxy method on (Ca, Mg, Zr)-Gd$_3$Ga$_5$O$_{12}$ garnet substrates. To study the effects of the thickness reduction on the saturation fields, the samples were etched in hot phosphoric acid for different periods of time. Then the measurements were performed to determine thickness, saturation field and the Faraday rotation angle. The experimental results for (100)-garnet films with out-of-plane and in-plane magnetization are summarized in Table 5-4. The data for (210)-garnet films with easy plane of magnetization as well as out-of-plane magnetization are given in Table 5-5. It was observed that for a (100)-oriented sample with an out-of-plane magnetization the reduction in the thickness of the film from 6 μm to 0.5 μm causes the saturation field to decrease monotonically from 125 Oe to 15 Oe (see Table 5-4). This significantly improves the spatial resolution and sensitivity of the MOI. In contrast, a (100)-oriented garnet film with in-plane magnetization and the saturation field of 337 Oe did not show a thickness dependence of the saturation field and the resolution did not improve with the thickness reduction, but became worse due to significant decrease in Faraday rotation angle. The effect of decreasing saturation field through the thickness reduction due to etching was also observed for the (210)-oriented samples of both types, with and without easy plane of magnetization. Etching of the easy plane sample from 5 μm down to 1.5 μm

reduced the saturation field from 60 Oe to 20 Oe, whereas for the sample without easy plane of magnetization reduction in the thickness from 6.5 μm down to 1.4 μm only caused a decrease in the saturation field from 109 Oe to 48 Oe (Table 5.5). The changes in the saturation fields for (210) easy plane and (100) out-of-plane samples are plotted in Fig. 5.7. As expected and apparent from Table 5-4 and Table 5-5, the Faraday rotation angle is practically proportional to the garnet film thickness.

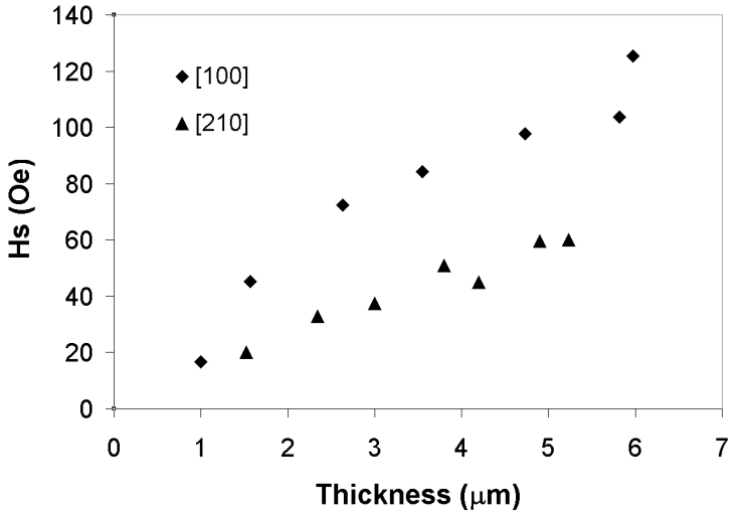

Fig. 5.7. Dependence of the saturation fields on the thickness of the samples.

During the experiments it has been observed that the reduction in the thickness of the garnet films affects their intrinsic domain structure. Fig. 5.8 illustrates the evolution of the domain structure of the out-of-plane garnet film grown on (100) substrate as the thickness of the film is reduced. Similar to our previous observations for (210) samples the size of the magnetic domains for the (100)-oriented samples also reduces with the

thickness up to certain point, after which the domains start increasing again and may form a so called single domain state.

Table 5-4. Dependence of the maximum Faraday rotation (θ_F) and the saturation field (H_S) on the thickness of the film (t) for the garnet films grown on (100) substrates.

Out of plane			In plane		
t (μm)	θ_F (deg)	H_S (G)	t (μm)	θ_F (deg)	H_S (G)
5.97	8.75	125.4	4.40	4.75	337
5.82	8.00	103.7	3.90	4.25	338
4.73	6.50	97.7	3.26	3.50	342
3.55	5.00	84.2	2.53	3.00	304
2.63	4.25	72.3	1.87	2.25	300
1.57	2.50	45.2	1.60	1.50	306
1.00	1.50	16.6	1.32	1.25	344
0.50	0.75	15.3			

Table 5-5. Dependence of the maximum Faraday rotation (θ_F) and the saturation field (H_S) on the thickness of the film (t) for the garnet films grown on (210) substrates.

Out of plane			Easy plane of magnetization		
t (μm)	θ_F (deg)	H_S (G)	t (μm)	θ_F (deg)	H_S (G)
6.53	7.15	109	5.23	6.25	60.0
6.15	7.00	103	4.90	5.25	59.6
5.46	6.75	98	4.20	5.00	45.1
4.06	5.06	89	3.80	4.25	50.9
3.53	3.69	81	3.00	3.25	37.4
2.32	2.47	65	2.34	2.50	33.0
1.40	1.46	48	1.52	1.25	20.1

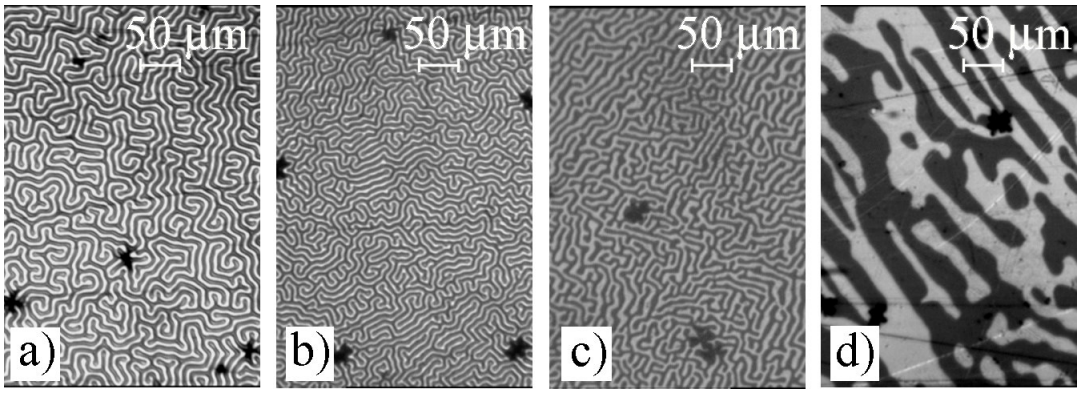

Fig. 5.8. Changes in the domain structure of the out-of-plane garnet film grown on (100) substrate with the film thickness reduction. Image (a) unetched, 6µm thick film, (b) 2.6̣3 µm thick film, (c) 1 µm thick film, and (d) 0.5̣µm thick film.

A DDS tape with submicron size recorded features has been used to test imaging capabilities of (100) etched garnet films and compare the results with those obtained for (210) oriented films. The images shown in Fig. 5.9 were obtained using etched, 1µm thick, (100)-oriented garnet film with out-of-plane magnetization (the domain structure of the film is shown in Fig. 5.8(c)). It can be observed from these images that in spite of the intrinsic domain structure of the film, fields from the DDS tape are strong enough to force magnetization in the garnet to replicate the patterns of the emanating magnetic fields. Further reduction in the film thickness changes the domain structure towards the single domain state (see Fig. 5.8(d)) but does not provide any noticeable improvement in imaging capabilities. It is apparent from Fig. 5.9 that the properly etched garnet films exhibit submicron imaging resolution.

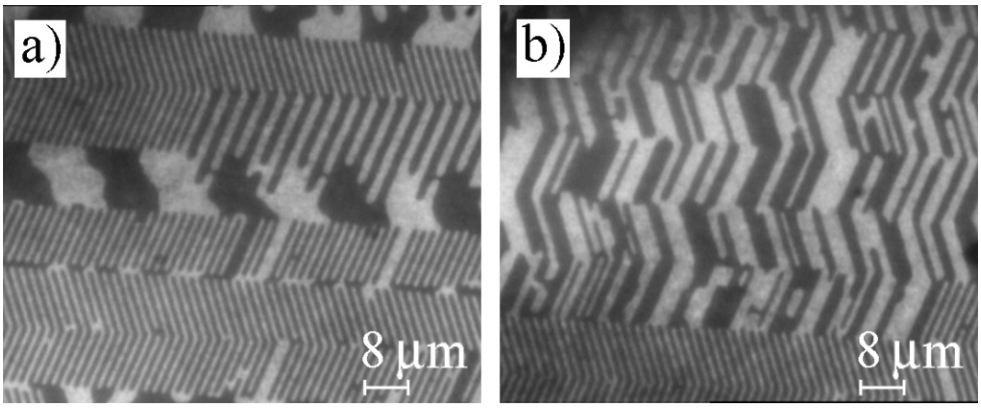

Fig. 5.9. Images of different parts of a DDS tape using etched 1 μm thick (100)-garnet film with out-of-plane magnetization.

The appreciable increase in sensitivity and imaging resolution can be explained as follows. It is well known that fringing magnetic fields caused by the periodic magnetization patterns exponentially decay from the tape surface. For this reason, it is essential to use very thin garnet films that can exclusively access the region where the magnetic fields are not yet reduced and more or less uniform over the garnet film thickness. On the other hand, the thinner the magneto-optically active layer, the smaller the amount of Faraday rotation, which is detrimental to the contrast and imaging resolution. Furthermore, there is another important factor that comes into play for the out-of-plane samples. The thickness reduction of garnet films affects local demagnetizing fields and, in this way, it makes it easier for the domains to switch. This explains why there is a drastic reduction in saturation fields for the etched out-of-plane (100) garnet films, while no such reduction has been observed for the etched in-plane (100) samples.

Garnet films with low growth-induced uniaxial anisotropy

This work has been performed in collaboration with Vincent J. Fratello from Integrated Photonics, Inc. It has been motivated by the study of the novel samples with small uniaxial anisotropy grown at Integrated Photonics by liquid phase epitaxy on (100)-oriented substrates. All these samples were grown under very similar conditions from two slightly different melts. Nevertheless, some of them show great potential for imaging applications despite high saturation fields (H_S) whereas others become usable only after etching to submicron thickness. The properties of the studied samples are summarized in Table 5-6, and the value of specific Faraday rotation was found to be about 1.5 deg/μm for all these samples.

Table 5-6. Properties of the garnet films with low growth-induced uniaxial anisotropy.

Sample	Thickness, t (μm)	$4\pi M_S$ (G)	H_S (Oe)	$\Delta a=a_s-a_f$ (Å)	Domain type
1-1	1.9	600	675	-0.0037	In-plane
2-1	1.8	380	458	-0.0019	Canted
2-2	4.4	380	358	-0.0016	Out-of-plane
2-3	6.0	400	365	+0.0011	Out-of-plane
2-4	4.0	331	256	+0.0105	Out-of-plane
3-1	2.0	480	590	-0.0005	In-plane

Sample 1-1 was grown from melt 1 and has in-plane magnetization orientation. The close up of the border of two large in-plane domains shows the presence of the finer domain structure with stripes in adjacent domains being oriented approximately at 90° with respect to each other (see Fig. 5.10). This type of domain structure suggests that the

positive growth-induced uniaxial anisotropy constant has smaller value than the magnetostrictive term that favors in-plane magnetization orientation. The presence of the fine striped domains indicates that the cubic anisotropy energy is comparable to the uniaxial and magnetostrictive terms. Furthermore, a relative orientation of the stripes at right angles across the in-plane domain wall suggests negative K_1 which introduces local minima along (111) directions and allows for the out-of-plane component of magnetization.

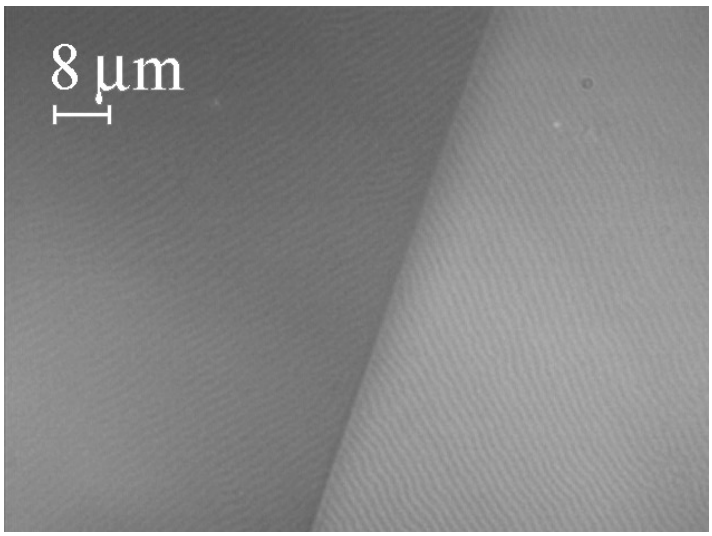

Fig. 5.10. Domain structure of sample 1-1.

Evaluation of the imaging capabilities of sample 1-1 was performed with a polarized light microscope using digital data storage (DDS) tape. A typical image obtained by using this sample is shown in Fig. 5.11. Despite the high saturation field H_S and the 2µm thickness of the film the recorded magnetic pattern is well resolved. The high sensitivity of this sample is attributed to the delicate balance of its anisotropies that

allows the small magnetic field from the DDS tape to switch the film magnetization between local minima.

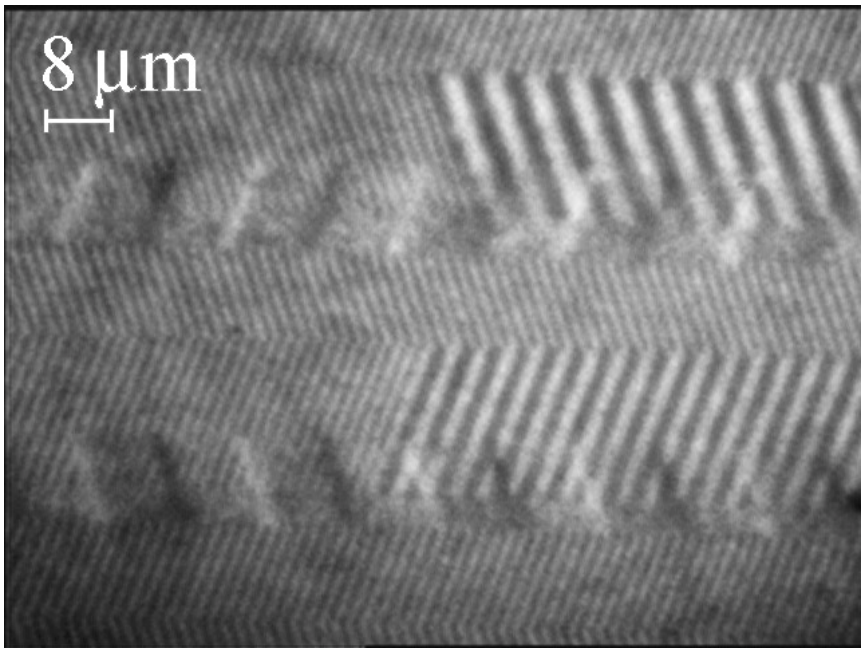

Fig. 5.11. Image of DDS tape obtained using sample 1-1.

Samples 2-1, 2-2, 2-3 and 2-4 were grown from melt 2 that has been modified from melt 1 in order to decrease the $4\pi M_S$ value. These samples range in the type of their domain structure from in-plane (sample 2-1) to strong out-of-plane (sample 2-4). It is interesting to note that samples 2-1 and 2-2 were grown at only slightly different undercooling, yet their domain structure is quite different (see Fig. 5.12). Sample 2-1 clearly shows presence of in-plane domains with superimposed finer stripe domain structure, as seen in Fig. 5.12(a). In this sense, it is similar to sample 1-1. Sample 2-2 (see Fig. 5.12(b)) does not reveal any sign of the presence of the large in-plane domains, but

shows domain alignment consistent with strong crystalline anisotropy. Apparently, the amount of stress due to lattice mismatch for the sample 2-2 was not sufficient to bring magnetization into the plane, whereas for the sample 2-1 it was just enough to obtain a canted magnetization state. This further reinforces the idea that the contribution to the total magnetic energy density from the uniaxial anisotropy is comparable to the cubic and magnetostrictive energy terms. Samples 2-3 and 2-4 both have a positive lattice mismatch. The domain structure for the sample 2-3 is almost identical to that of 2-2 whereas the sample 2-4 has serpentine domains typical for the strong out-of-plane magnetization.

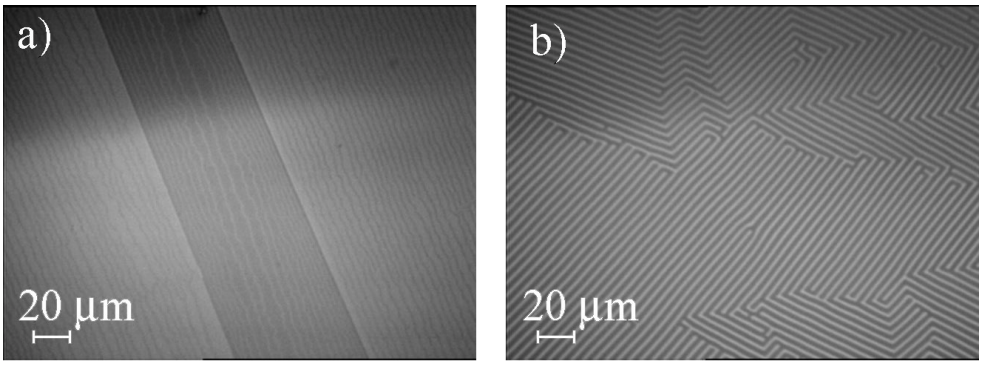

Fig. 5.12. Domain structures of the a) canted sample, 2-1; b) out-of-plane sample, 2-2.

Samples 2-1 and 2-2 were used to test their imaging capabilities by using the same set up as for the sample 1-1. The images are shown in Fig. 5.13. The quality of the image for the sample 2-1 is very high whereas the domain pattern in sample 2-2 completely obscures the data pattern of the tape.

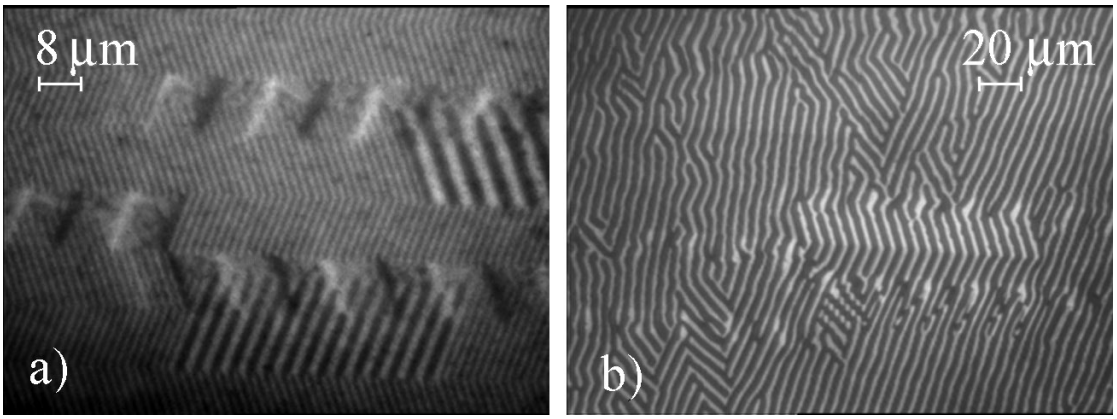

Fig. 5.13. Images of the DDS tape captured using a) sample 2-1, and b) sample 2-2.

Since the difference in the growth parameters between the two samples is very small, one of the possible explanations for such different imaging capabilities could be attributed to a large difference in the film thickness which affects local demagnetizing fields. Therefore it was interesting to investigate how the properties of sample 2-2 change with thickness reduction. A set of etching experiments was conducted in order to gradually decrease the thickness of the film and observe the changes in the domain pattern as well as saturation field H_S. The results are summarized in Table 5-7. Only a slight decrease in the saturation field was observed for sample 2-2 which is in contrast to the large changes in H_S for the samples with strong growth-induced uniaxial anisotropy. The imaging capabilities of the film improved somewhat when the thickness was reduced to about 1µm, as shown in Fig. 5.14. A similar etching experiment was conducted for the sample 2-3 and the results obtained are very similar to those for sample 2-2.

Table 5-7. Properties of the etched sample 2-2

Thickness, t (μm)	domain period (μm)	H_S (Oe)
4.4	5.0	358
4.0	5.6	378
3.3	5.2	369
2.8	4.9	350
2.3	4.5	325
1.5	3.1	316
0.9	1.3	304

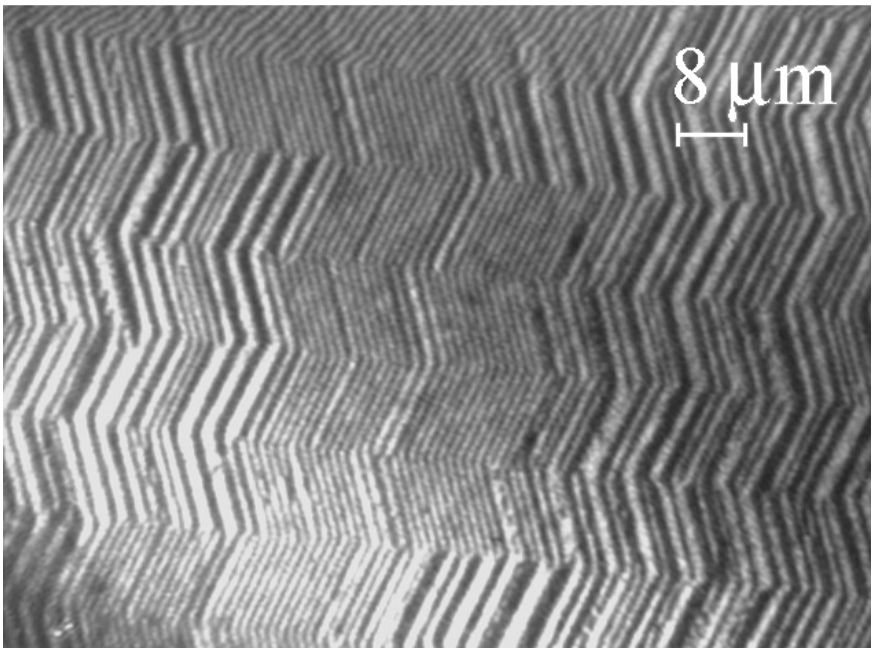

Fig. 5.14. Image of the DDS tape obtained using etched sample 2-2 of thickness 0.9 μm.

The magnetic energy density function was studied in order to investigate if the small differences in the lattice mismatch between the samples can cause significant

differences of their imaging capabilities. The following equation was used for the numerical evaluation

$$E = -K_g cos^2\theta + K_1(sin^2\theta\, cos^2\theta + sin^4\theta\, cos^2\varphi sin^2\varphi) + \frac{3}{2}\lambda_{100}\sigma_0 cos^2\theta\,, \qquad (5.5)$$

where the magnetostrictive coefficient of the material λ_{100}= -2·10^{-6}, and the amount of the stress σ_0 was calculated for different lattice mismatch [Han78]. The values of the cubic and growth induced anisotropy coefficients were obtained by fitting to the ferromagnetic resonance measurement data and are given in Table 5-8.

Table 5-8. Anisotropy constants

Sample	K_S (erg/cc)	K_1 (erg/cc)	K_g (erg/cc)
1-1	-3588	-3342	3146
2-1	-2505	-2087	1129
2-2	-1354	-1860	1898
3-1	-338	-1566	-827

It is important to note that for these samples the values of the growth induced anisotropy constant K_g, the cubic anisotropy constant K_1 and the stress anisotropy K_S = -3/2 λ_{100} σ_0 are of the same order of magnitude. Therefore the contributions from the stress and cubic anisotropies cannot be neglected as is typically done. The relatively significant value of the cubic anisotropy introduces minima of the magnetic energy density at θ = 45°, and θ = 135°. This may either increase or decrease the sensitivity of the film to the applied field depending on the value of the uniaxial anisotropy. Also the fact that these constants are

very small makes the stress contribution important and allows control of the uniaxial anisotropy by changing the lattice mismatch.

The dependence of the magnetic free energy density on polar angle θ for samples 1-1, 2-2 and 3-1 is plotted in Fig. 5.15. The azimuth angle φ was fixed at 45° since the cubic anisotropy energy term is the smallest for this value.

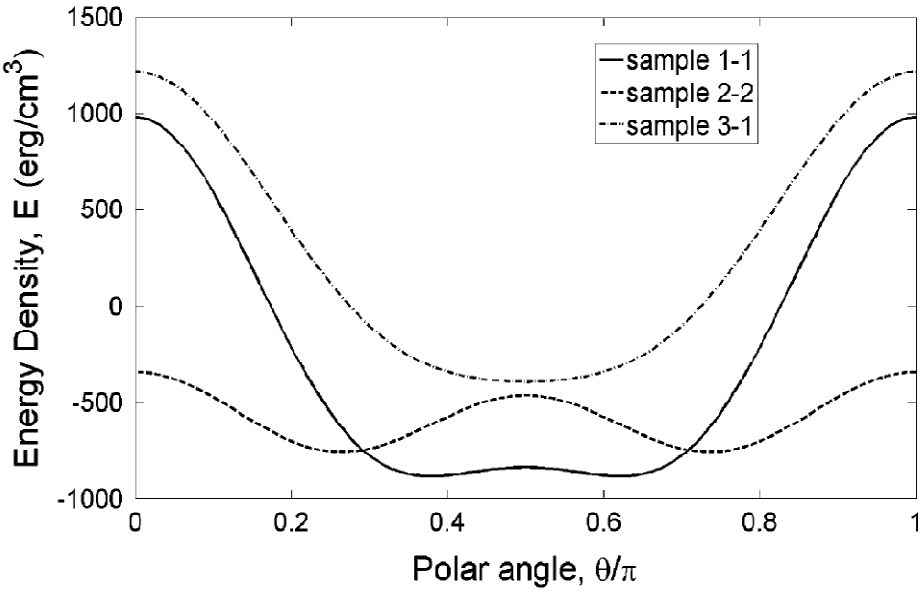

Fig. 5.15. The dependence of the magnetic free energy density on the polar angle θ. The azimuth angle $\varphi = \pi/4$. At $\theta/\pi = 0.5$ the magnetization is oriented in-plane.

The plot shows two deep energy minima where the magnetization is pinned for sample 2-2. At the same time samples 1-1 and 3-1 have flat energy minima where the magnetization is free to move within relatively wide range of angles θ. This kind of the energy density dependence explains why some of the samples with low growth-induced anisotropy are very good magneto-optical imagers whereas others are not.

Plasmon resonance enhancement of Faraday rotation in thin garnet films

This section presents the results of experimental work on garnet films grown by liquid phase epitaxy (LPE) over (100)-oriented SGGG substrates partially populated with gold nanoparticles.

First we studied the formation of the gold nanoparticles on (100) GGG substrates. In order to produce nanoparticles a thin layer of gold was sputtered on a clean substrate in a "checkerboard" pattern and subsequently annealed at various temperatures in ambient atmosphere. Optimal thickness of the sputtered gold layer was determined by partially dipping the substrate with 6nm thick gold layer into hot (about 100°C) orthophosphoric acid. Visual inspection suggests that some amount of gold was removed as a result of substrate etching. The substrate was annealed and studied using AFM. The AFM images of the substrate surface with gold before (Fig. 5.16a) and after (Fig. 5.16b) etching are shown in the figure below.

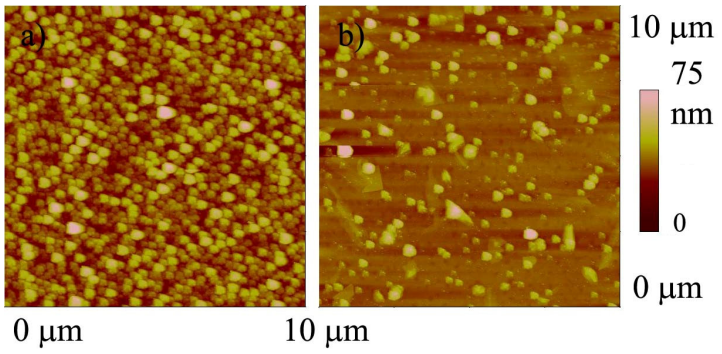

Fig. 5.16. Surface of the garnet substrate with gold a) before and b) after etching.

It can be seen from Fig. 5.16 that thinner layer of gold results in larger spacing and smaller size of gold nanoparticles. As a result of studies of nanoparticle formation depending on the annealing temperature and gold layer thickness it was found suitable for further experiments to use layers of gold of thickness approximately 4 nm and annealed at 850°C. These conditions result in the formation of nanoparticles AFM image of which is shown in Fig. 5.17.

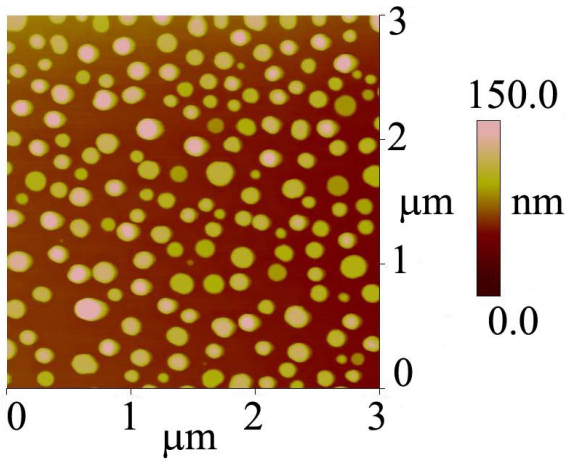

Fig. 5.17. AFM image of gold nanoparticles formed from 4nm layer of gold annealed at 850°C.

The diameter of the particles varies from 10 to 250 nm and the majority of them have the diameter less than 100 nm. The color bar to the right of the figure provides the scale for the height of the particles. The particle height is about 0.8-1.0 of particle radius.

Light transmission experiments were conducted by using a J.A. Woollam VASE variable angle spectroscopic ellipsometer to measure the transmission coefficients of SGGG substrates in the areas with and without gold nanoparticles. Fig. 5.18 presents the

results of these measurements. The difference in the transmission coefficients can be attributed to absorption of light energy caused by plasmon resonances induced in the gold nanoparticles. The data suggest that plasmon resonances in gold nanoparticles occur around the wavelength of 600nm where a clearly defined minimum can be seen. The minimum in transmitted light is due to the appreciable increase in energy losses caused by strong electric fields inside gold nanoparticles induced at plasmon resonances as well as by the imaginary part of their dielectric permittivity. The observed resonance wavelength (600nm) is consistent with the theoretical analysis presented in Chapter 4 where it was found that plasmon resonances in hemispherical nanoparticles occur at the wavelength range between 580 nm and 620 nm for different height to radius ratios. We have also performed the simulations for an ensemble of nanoparticles separated by various distances and found that when the spacing-to-diameter ratio exceeds 0.3 the resonance wavelength is the same as for a single nanoparticle. It is also worthwhile to remind that the resonance wavelength is scale invariant. This means that the resonance wavelength depends on the shape of nanoparticles but not their geometrical dimensions provided that the resonance wavelength is quite large in comparison with particle dimensions. This scale invariance implies that almost self-similar gold nanoparticles may resonate at practically the same wavelength and, for this reason, the curve presented in the insert of Fig. 5.18 reflects the collective effect of plasmon resonances in gold nanoparticles.

By using the liquid phase epitaxy technique, thin garnet films of (Bi, Pr, Y, $Gd)_3(Fe, Ga)_5O_{12}$ composition have been grown on (100)-oriented SGGG substrates

partially populated with gold nanoparticles. Thus, gold nanoparticles have been embedded in epitaxially grown garnet films. It is not immediately clear how the growth process affected the shape of the gold nanoparticles or whether they even survived as particles.

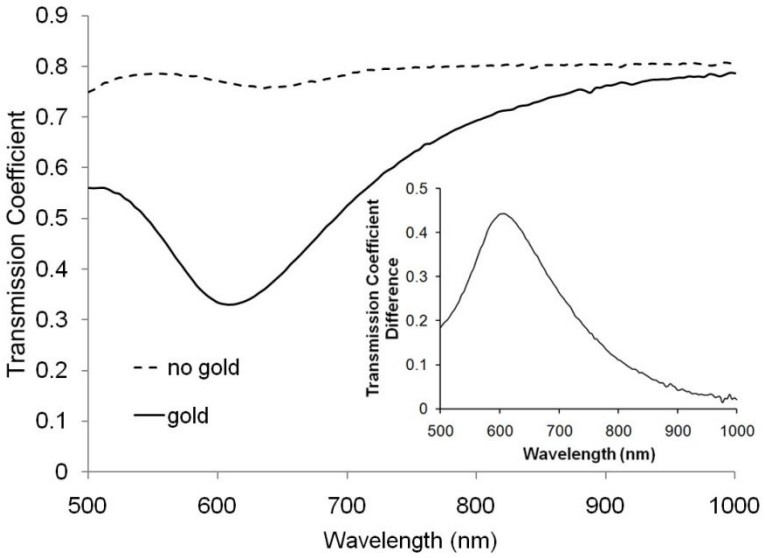

Fig. 5.18. Transmission coefficients of the garnet substrate with and without gold.

To investigate this matter, x-ray diffraction measurements have been conducted using PANalytical X'Pert PRO MRD system with x-ray source emitting at the CuKα line with wavelength λ=0.15405nm. These measurements have clearly revealed the presence of gold (111) peak near 19.1°, both prior to and after the epitaxial growth of garnet film (see Fig. 5.19).This suggests that gold nanoparticles withstood the growth process in some crystalline form. However, their shape may be appreciably changed as well as their mutual separations. It is particularly interesting to note the slight difference in the

location of the sub-gold and sub-gold-film peaks. Both measurements gave exactly the same location of the substrate peak, which indicates that the shift in the location of the gold peak is not due to some kind of misalignment of the samples. There are two ways to explain such a shift; one explanation is that the shift is due to the elastic strain in the gold on top of which garnet film is grown. Another explanation is that the gold is alloying with something else in the melt (for example platinum). Given that the shift in the location of the peaks is about 1% of the gold lattice parameter both of the above mentioned options are quite possible.

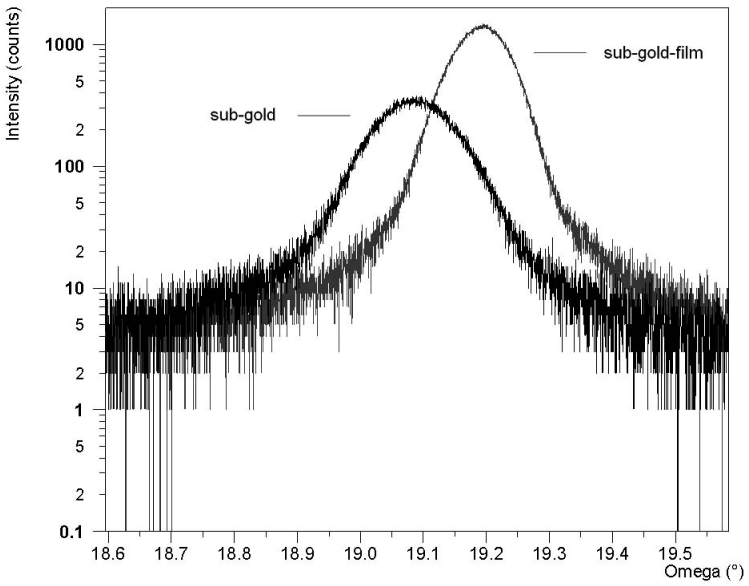

Fig. 5.19. XRD peaks for gold (111) reflection.

Light transmission experiments have been conducted to measure the transmission coefficients in the areas with and without gold nanoparticles embedded between the substrate and the film. To avoid (or minimize) the ambiguity associated with the

variations in the thickness and composition of epitaxially grown garnet films, the measurements have been performed in pairs of adjacent areas located on different sides of the boundary between the parts of the samples populated and not populated with gold nanoparticles. This is illustrated by Fig. 5.20, where these pairs of adjacent areas are marked as p1-1 and p1-2, p2-1 and p2-2, p3-1 and p3-2. Fig. 5.21 presents the results of the transmission coefficient measurements for adjacent areas p1-1 and p1-2, while the difference in the transmission coefficients in these adjacent areas is shown in Fig. 5.22. The differences in transmission coefficients shown in Fig. 5.22 can be attributed to the presence of gold nanoparticles that survived the epitaxial growth of garnet film.

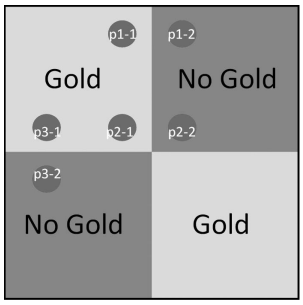

Fig. 5.20. Outline of the gold deposition pattern and measurement points.

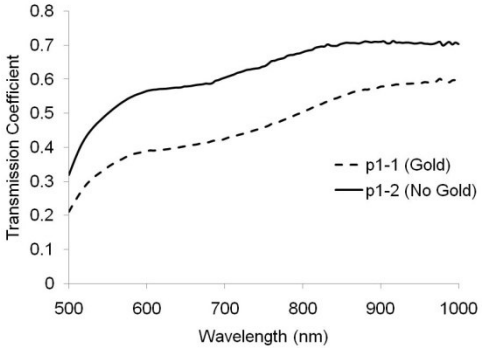

Fig. 5.21. The results of the transmission coefficient measurements for adjacent points p1-1 and p1-2.

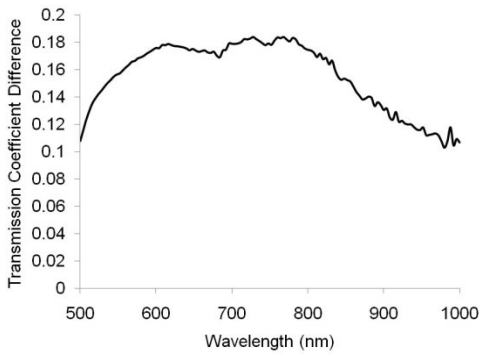

Fig. 5.22. Difference of the transmission coefficient measurements for adjacent points p1-1 and p1-2.

It is conceivable that these transmission differences are due to plasmon resonances in gold nanoparticles embedded in epitaxially grown garnet films. It is also apparent that the solid curve shown in Fig. 5.18 is quite different in comparison with the curves shown in Fig. 5.22. This can be caused by modification of the shape of gold nanoparticles and their mutual locations as a result of the epitaxial growth process. The "broad" plasmon resonances exhibited by curves shown in Fig. 5.22 may be beneficial because they may eventually lead to the Faraday rotation enhancement in a wide wavelength (frequency) range.

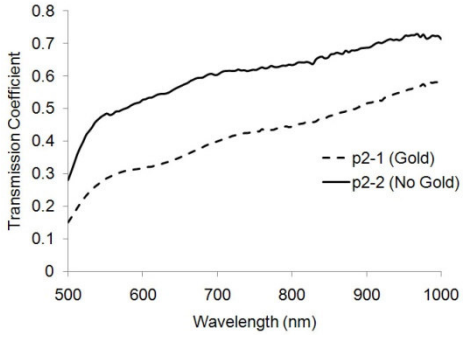

Fig. 5.23. The results of the transmission coefficient measurements for adjacent points p2-1 and p2-2.

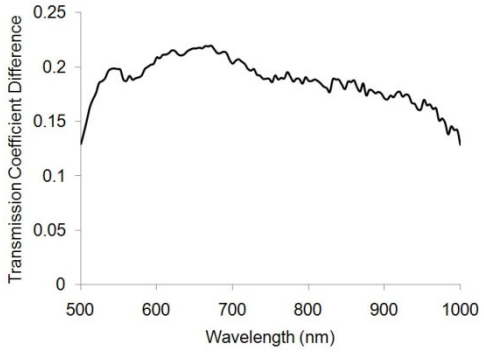

Fig. 5.24. Difference of the transmission coefficient measurements for adjacent points p2-1 and p2-2.

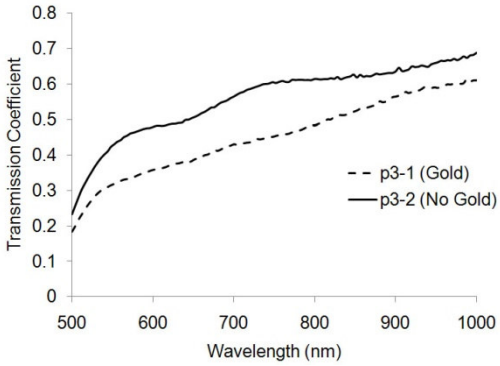

Fig. 5.25. The results of the transmission coefficient measurements for adjacent points p3-1 and p3-2.

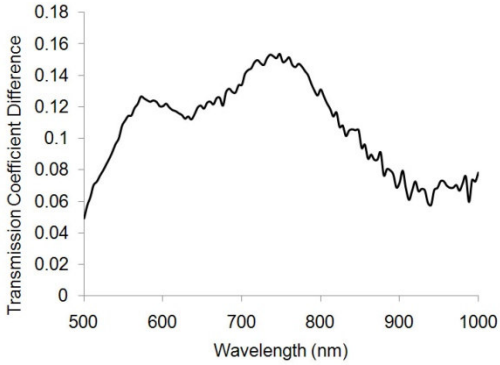

Fig. 5.26. Difference of the transmission coefficient measurements for adjacent points p3-1 and p3-2.

Similar results were obtained for pairs of points p2-1 / p2-2 (see Fig. 5.23 and Fig. 5.24) and p3-1 / p3-2 (see Fig. 5.25 and Fig. 5.26).

The Faraday rotation enhancement has been tested for pairs of adjacent regions shown in Fig. 5.20. The testing has been performed by using stabilized 532nm and 633nm lasers for the applied magnetic fields of 2.6kG. The results of measurements are summarized in the Table 5-9 where the Faraday rotations normalized by local thickness of epitaxially grown garnet film are reported.

Table 5-9. Faraday rotation measurements.

	Garnet Film Thickness (μm)	*FR/thick, Increase @633nm*	*FR/thick, Increase @532nm*
p1-1	0.34	0.74°/μm	2.85°/μm
Gold		13.6%	9.0%
p1-2	0.34	0.65°/μm	2.62°/μm
No Gold			
p2-1	0.39	0.85°/μm	2.95°/μm
Gold		12.8%	9.9%
p2-2	0.38	0.75°/μm	2.68°/μm
No Gold			
p3-1	0.35	0.89°/μm	2.97°/μm
Gold		13.2%	11.1%
p3-2	0.46	0.78°/μm	2.67°/μm
No Gold			

It is evident from the Table 5-9 that the Faraday rotation enhancement between 9% and 13% has been observed in the regions with gold (p1-1, p2-1, p3-1). The variations in the specific Faraday rotation for different points with no gold can be attributed to the large-

scale nonuniformity in the film composition. It is also apparent that the Faraday rotation enhancement presented in the Table 5-9 occurs in the wide wavelength range which is consistent with “broad” plasmon resonance curves shown in Fig. 5.22.

It may be conjectured that Faraday rotation enhancements shown in Table 5-9 are negatively affected by the diamagnetic nature of gold. To investigate this issue, optical curves representing the Faraday rotation versus magnetic field have been measured. One such measured curve for 633 nm wavelength and the location marked as p2-1 is shown in Fig. 5.27.

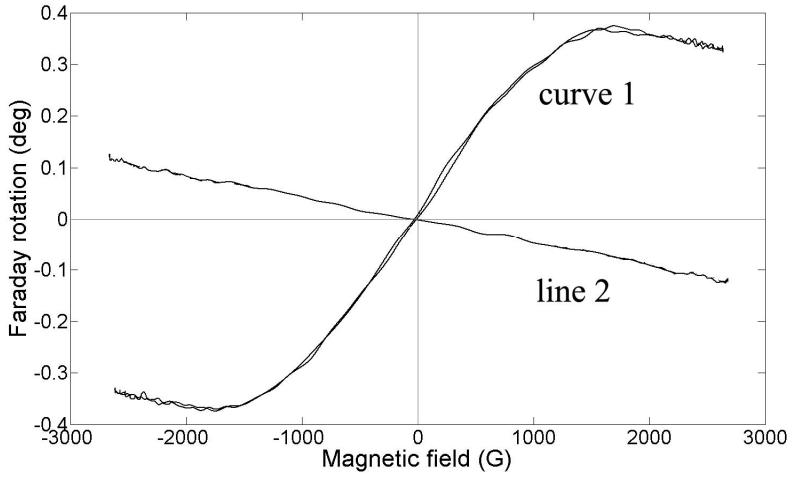

Fig. 5.27. Optical hysteresis loops for p2-1 of the area with gold nanoparticles (curve 1) and substrate with gold nanoparticles and no film grown (line 2).

It is apparent from Fig. 5.27 that for sufficiently large magnetic fields the Faraday rotation exhibits the monotonic decrease (see curve 1). To ascertain that this decrease can be fully attributed to the diamagnetic nature of gold, the Faraday rotation vs magnetic

field has been measured for a SGGG substrate with only 5 nm thick layer of gold evaporated on it, i.e. without (LPE) growth of a garnet film. The measurement results are presented by the line 2 on Fig. 5.27 and they reveal practically the same negative slope of this line as for the curve 1 for sufficiently large magnetic fields. This suggests that the intrinsic Faraday rotation enhancement of garnet films caused by plasmon resonance electric fields may be concealed and masked by the diamagnetic nature of gold. The intrinsic Faraday rotation of the garnet can be obtained by "subtracting" the line 2 from the curve 1. This intrinsic Faraday rotation is shown as the curve 1 on Fig. 5.28. On the same Figure, the curve 2 represents the optical measurements performed for the location p2-2 (region with no gold).

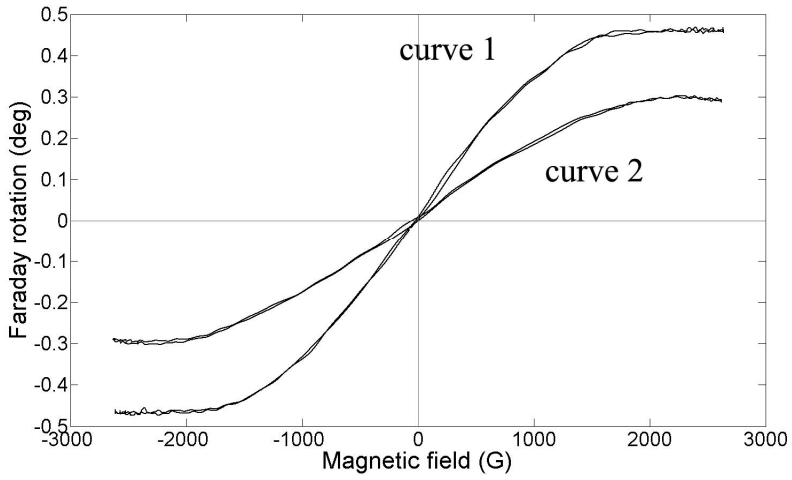

Fig. 5.28. Intrinsic (curve 1) and measured (curve 2) optical hysteresis loops for the areas with and without gold.

The comparison of the curves 1 and 2 shown in Fig. 5.28 suggests that for sufficiently large magnetic fields plasmon resonances in gold nanoparticles embedded in garnet films result in almost 50% increase in the saturation values of the Faraday rotation.

Another interesting observation is that the presence of gold seems to affect effective uniaxial anisotropy which manifests itself in the reduction of the saturation field H_S (see Fig. 5.29). The exact mechanism is not known but one possible explanation is that the thickness of the actual garnet film is smaller and therefore a demagnetizing field is larger, which in turn affects the effective uniaxial anisotropy.

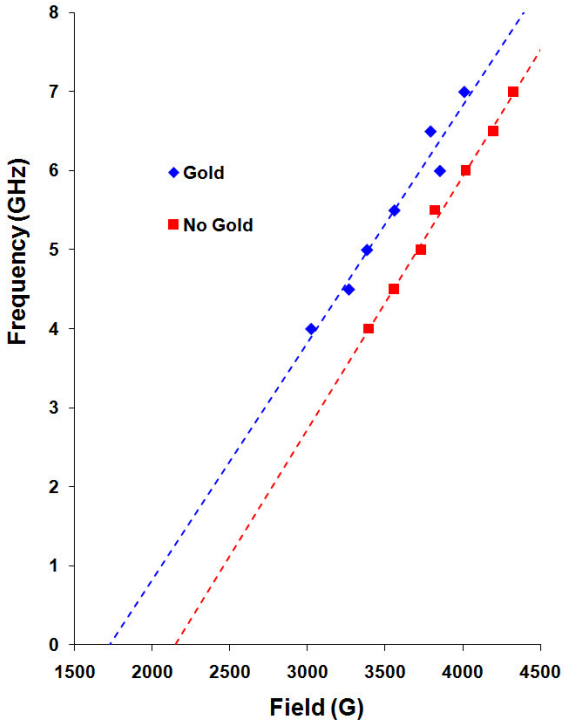

Fig. 5.29. Results of the FMR measurements.

It is apparent that detrimental effects of the gold diamagnetic nature on the overall plasmon resonance enhancement of Faraday rotation of garnet films can be reduced by growing garnet films with small saturation magnetic fields. One possible way of achieving this is by using (210)-oriented substrates. This issue will be investigated in our future research.

Conclusions and future work

This proposal discusses the use of magnetic single crystal Bi-substituted garnet thin films as magneto-optical indicators for imaging of weak stray magnetic fields. The design of the imagers is based on iron garnet films grown by liquid phase epitaxy. Their principle of operation employs the Faraday effect in which the rotation of the plane of polarization of transmitted light depends on the applied magnetic field. The advantages of these indicators are high resolution, high contrast, possibility of the imaging of magnetic fields in a wide range of magnitudes, as well as non-scanning and non-contaminating nature of the imaging technique.

A lot of research was done on growth and characterization of the samples grown on (210)-oriented substrates. Significant results were achieved in the area of the melt design and understanding of the various factors that affect the properties of the grown garnet films. Very interesting and unique results were obtained on imaging of the magnetic field patterns using unetched in-plane and etched out-of-plane garnet films. The research performed on samples with (210) substrate orientation shows great promise for the MOI applications because of the existence of the easy plane of magnetization. Currently the growth of the films with such easy magnetization plane is difficult because of the high complexity of the growth process and unavailability of the data on the anisotropy constants for rare-earth elements when coupled with Bi in (210) oriented films. So far we can only estimate the values of the anisotropy constants based on the research performed for (111) oriented films [Frat86]. Therefore one possible direction of the future research work is to determine the growth induced uniaxial and the cubic

anisotropy constants for different rare-earth when coupled with bismuth in (210) oriented films.

Another interesting part of the research was the joint project on investigation of the magnetic garnet films with near zero uniaxial anisotropy grown on (100) substrates. This project has been performed in collaboration with Dr. Vincent Fratello formerly from Integrated Photonics Inc. The essence of it is that in case of very small uniaxial anisotropy the contributions of the crystalline anisotropy energy term and the magnetostrictive term must be taken into account. The influence of these terms on the magnetic free energy density allows growth of the samples that are excellent for the imaging of stray magnetic fields. This of course requires very precise control of the melt composition and growth parameters (particularly growth temperature stability). We have demonstrated that samples with near zero uniaxial anisotropy can be used for magneto-optical imaging applications. We have also gathered experimental data on the values of the anisotropy fields and their dependence on the melt composition and growth conditions. This opens another promising direction for future research. New melt compositions need to be developed that would allow improving properties of the samples with low growth-induced anisotropy.

A new project on the studies of the plasmon resonance enhanced Faraday effect was started. We demonstrated possibility of LPE growth of thin garnet films on top of the substrate with gold nanoparticles. We proved that the gold survives LPE growth even though it is not entirely clear how the growth process affects the shape of the

nanoparticles. Peaks of absorption were experimentally found at frequencies of the plasmon resonances for multiple samples. The angle of Faraday rotation was measured in the areas with and without gold for the same sample and it was found that there is indeed a significant (about 50%) increase in Faraday effect after the diamagnetic contribution of gold is removed. Possible directions of research on the plasmon resonance enhancement of Faraday rotation include development of melts that would allow growth of samples with low saturation fields in order to reduce diamagnetic masking effect, growth of ultrathin garnet films that would be affected by the excited electric fields across their whole thickness, growth of multilayer films with the gold nanoparticles being embedded in-between successive layers.

Bibliography

[BaWa88] L. Baselgia, M. Warden, et al., "Derivation of the resonance frequency from the free energy of ferromagnets", *Physical Review B*, **38**, 2237 (1988).

[BlaN72] S.L. Blank, J.W. Nielsen, "Growth of magnetic garnets by liquid-phase epitaxy", *Journal of Crystal Growth*, **17**, 302 (1972).

[BuDu03] V.I. Butrim, S.V. Dubinko, and Yu.N. Mitsai, "Anisotropy and phase states of garnet ferrite films with misoriented surfaces", *Physics of the Solid State*, **45**, 1102 (2003).

[DoBu93] P.C. Dorsey, S.E. Bushnell, R.G. Seed, and C. Vittoria, "Epitaxial yttrium iron garnet films growth by pulsed laser deposition", *Journal of Applied Physics*, **74**, 1242 (1993).

[Esch81] A.H. Eschenfelder, "Magnetic Bubble Technology", *Springer-Verlag*, New York (1981).

[Fon56] S. Foner, "Vibrating Sample Magnetometer", *Review of Scientific Instruments*, **27**, 548 (1956).

[Fon59] S. Foner, "Versatile and Sensitive Vibrating Sample Magnetometer", *Review of Scientific Instruments*, **30**, 548-557 (1959).

[Frat86] V. J. Fratello, S. E. G. Slusky, C. D. Brandle and M. P. Norelli, "Growth-Induced Anisotropy in Bismuth-Rare Earth Iron Garnets", *Journal of Applied Physics*, **60**, 2488 (1986).

[Frat89] V. J. Fratello, S.J. Licht, and M.P. Norelli, "Effect of melt composition on Bi incorporation in iron garnets", *Journal of Crystal Growth*, **97**, 657 (1989).

[Fuji08] R. Fujikawa, A. V. Baryshev, J. Kim, H. Uchida, and M. Inoue, J. Appl. Phys. 103, 07D301 (2008).

[Grif46] J.H.E. Griffiths,"Anomalous High-frequency Resistance of Ferromagnetic Metals", *Nature*, **158**, 670 (1946).

[HaKru84] P. Hansen and J. P. Krumme, "Magnetic and magneto-optical properties of garnet films", *Thin Solid Films*, **114**, 69 (1984).

[Han78] P. Hansen, "Magnetic Anisotropy and Magnetostriction in Garnets", *Physics of Magnetic Garnets*, North-Holland, Amsterdam, pp. 56-133, 1978.

[HaWi83] P. Hansen, K. Witter, and W. Tolksdorf, "Magnetic and Magneto-optical properties of bismuth-substituted gadolinium iron garnet films", *Phys. Rev. B.*, **27**, 4375 (1983).

[Hib85] T. Hibiya, Y. Morishige, J. Nakashima, "Growth and characterization of Liquid-phase epitaxial Bi-substituted iron garnet films for magneto-optic applications", *Japan. J. Appl. Phys.*, **24**, 1316 (1985).

[Hol04] C. Holthaus, "Development of sensitive indicators for magneto-optical pattern recognition", *PhD Dissertation Thesis*, University of Osnabrück (2004).

[Kahn69] F. J. Kahn, P. S. Pershan, and J. P. Remeika, "Ultraviolet Magneto-Optical Properties of Single-Crystal Orthoferrites, Garnets, and other Ferric Oxide Compounds", *Phys.Rev.*, **186** (2), 891 (1969).

[KanOk87] M. Kaneko, T. Okamoto, H. Tamada and K. Sako," A low-loss 0.8-mum band optical isolator using highly Bi-substituted LPE garnet film", *IEEE Trans. Magn.*, 23, 3482 (1987).

[KaPe69] F.J. Kahn, P.S. Pershan, and J.P. Remeika, "Ultraviolet Magneto-Optical Properties of Single-Crystal Orthoferrites, Garnets, and Other Ferric Oxide Compounds", *Physical Review*, **186**, p.891 (1969).

[Kitt47] C. Kittel, "Interpretation of Anomalous Larmor Frequencies in Ferromagnetic Resonance Experiment", *Physical Review*, **71**, 270 (1947).

[KraDo07] C. S. Krafft, J. B. Dottellis, US Patent No. 7 239 332 B1, (2007).

[KraST11] C. Krafft, S. Tkachuk, G. Lang, D. Bowen, I.D. Mayergoyz, "Magneto-Optic Indicator Films for Forensics (invited)", on-line publication in *MRS Online Proceedings (part of Cambridge Journals Online),* January 2011.

[LaLi84] L.D. Landau and E.M. Lifshitz, "Electrodynamics of continuous media", *Pergamon Press*, New York, 1984.

[MaRu77] D. Mateika, and C. Rusche, "Coupled substitution of gallium by magnesium and zirconium in single crystals of gadolinium gallium garnet", *Journal of Crystal Growth*, **42**, 440 (1977).

[May07] I.D. Mayergoyz, Z. Zhang, and G. Miano, Phys. Rev. Lett. 98, 147401 (2007).

[May10] I.D. Mayergoyz, G. Lang, L. Hung, S. Tkachuk, C. Krafft, and O. Rabin, J. Appl. Phys., 107, 09A925 (2010).

[MiDu00] R.M. Mikherskii, S.V. Dubinko, "Epitaxial Garnet Ferrite Films with Anisotropy of the Inclined Easy Plane Type", Tech Phys Lett., 26, 265 (2000).

[Niel58] J. W. Nielsen, E. F. Dearborn, "The growth of single crystals of magnetic garnets", *Journal of Physics and Chemistry of Solids*, **5**, 202 (1958).

[Niel76] J. W. Nielsen, "Bubble Domain Memory Materials", *IEEE Trans. Mag.*, **12**, 327 (1976).

[Nist06] I. Nistor, "Development of magnetic field sensors using Bismuth-substituted garnets thin films with in-plane magnetization", *PhD Dissertation Thesis*, University of Maryland (2006).

[RoBo71] M. Robinson, A.H. Bobeck, and J.W. Nielsen, "Chemical Vapor Deposition of Magnetic Garnets for Bubble-Domain Devices", *IEEE Transactions on Magnetics*, **7**, 464 (1971).

[Sak67] J. J. Sakurai, *Advanced Quantum Mechanics*, (Addison-Wesley, Reading, MA, 1967).

[Tom06] S. Tomita, T. Kato, S. Tsunashima, S. Iwata, M. Fujii, and S. Hayashi, Phys. Rev. Lett. 96, 167402 (2006).

[UcMa09] H. Uchida, Y. Masuda, R. Fujikawa, A. V. Baryshev, and M. Inoue, J. Magn. Magn. Mater. 321, 843 (2009).

[Val90] K. M. Mukimov, B. Y. Sokolov, U.V. Valiev, "The Faraday Effect of rare-earth ions in garnets", *Physica Status Solidi A-Applied Research*, **119**, 307 (1990).

[Wem74] S. H. Wemple, S. L. Blank and J. A. Seman, "Optical properties of epitaxial iron-garnet thin films", *Phys. Rev. B*, **9**, 2134 (1974).

[Wet76] W. Wettling, "Magneto-optics of ferrites", *Journal of Magnetism and Magnetic Materials*, **3**, pp.147-160 (1976).

[WoRe67] D. L. Wood and J. P. Remeika, "Effect of impurities on the optical properties of yttrium iron garnet", *Jour. Appl. Phys.*, **38**, 1038 (1967).

[www-lar] http://www.larsenglish.com/magneticresonance

[YaBo47] W.A. Yager, R.M. Bozorth, "Ferromagnetic Resonance at Microwave Frequences", *Physical Review*, **72**, 80 (1947).

[Zhan04] J. Zhang, “Growth and FMR characterization of in-plane magnetization garnet thin films”, *Master Thesis*, University of Maryland (2004).

[ZveKo97] A. K. Zvezdin and V. A. Kotov, “Modern Magnetooptics and Magnetooptical Materials”, *Institute of Physics Publishing*, Bristol and Philadelphia, p. 163, 1997.